

DTIC FILE COPY

4

REPORT SD-TR-88-38

AD-A211 528

Three-Dimensional, Two-Phase, Transonic, Canted Nozzle Flows

Prepared by

I-SHIH CHANG
Engineering Group
The Aerospace Corporation
El Segundo, CA 90245-4691

DTIC
ELECTE
AUG 21 1989
S D D

2 December 1988

Prepared for

SPACE DIVISION
AIR FORCE SYSTEMS COMMAND
Los Angeles Air Force Base
P.O. Box 92960
Los Angeles, CA 90009-2960

*Original contains color
plates: All DTIC reproductions
will be in black and
white*

APPROVED FOR PUBLIC RELEASE;
DISTRIBUTION UNLIMITED

89 8 21 110

UNCLASSIFIED

SECURITY CLASSIFICATION OF THIS PAGE

REPORT DOCUMENTATION PAGE				
1a REPORT SECURITY CLASSIFICATION Unclassified		1b RESTRICTIVE MARKINGS		
2a SECURITY CLASSIFICATION AUTHORITY		3 DISTRIBUTION / AVAILABILITY OF REPORT Approved for public release; distribution unlimited		
2b DECLASSIFICATION / DOWNGRADING SCHEDULE				
4 PERFORMING ORGANIZATION REPORT NUMBER(S) TR-0089(4530-04)-1		5 MONITORING ORGANIZATION REPORT NUMBER(S) SD-TR-89-38		
6a NAME OF PERFORMING ORGANIZATION The Aerospace Corporation		6b OFFICE SYMBOL (if applicable)	7a NAME OF MONITORING ORGANIZATION Space Division Air Force Systems Command	
6c ADDRESS (City, State, and ZIP Code) 2350 E. El Segundo Blvd. El Segundo, CA 90245-4691		7b ADDRESS (City, State, and ZIP Code) Los Angeles Air Force Base P. O. Box 92960 Los Angeles, CA 90009-2960		
8a NAME OF FUNDING / SPONSORING ORGANIZATION Space Division		8b OFFICE SYMBOL (if applicable) SD/CLVD	9 PROCUREMENT INSTRUMENT IDENTIFICATION NUMBER F04701-88-C-0089	
8c ADDRESS (City, State, and ZIP Code) See 7b		10 SOURCE OF FUNDING NUMBERS		
		PROGRAM ELEMENT NO	PROJECT NO	TASK NO
				WORK UNIT ACCESSION NO.
11 TITLE (Include Security Classification) Three-Dimensional, Two-Phase, Transonic, Canted Nozzle Flows				
12 PERSONAL AUTHOR(S) I-Shih Chang				
13a. TYPE OF REPORT Final	13b TIME COVERED FROM 1986 TO 1988		14 DATE OF REPORT (Year, Month, Day) 2 December 1988	15 PAGE COUNT 57
16. SUPPLEMENTARY NOTATION				
17 COSATI CODES			18 SUBJECT TERMS (Continue on reverse if necessary and identify by block number) Gas-particle, Two-phase, Nozzle, Transonic Flow, Computational Method	
FIELD	GROUP	SUB-GROUP		
19 ABSTRACT (Continue on reverse if necessary and identify by block number) A time-dependent numerical scheme, in conjunction with a three-dimensional, body-fitted coordinate transformation technique, is utilized for the solution of subsonic-transonic-supersonic flows: both gas-only, one-phase and fully coupled, gas-particle, two-phase flows inside three-dimensional canted nozzles of arbitrary configurations. The emphasis of the study is placed upon the transonic flow solution, which has been a bottleneck in many three-dimensional nozzle flow studies. Precise interpretation of flow variables in a canted nozzle is obtained through the simultaneous solution of multiple flow regions for motor aft closure and nozzle with two different coordinate centerlines. Numerical calculations are carried out for the seven-segment Titan IV solid rocket motor aft closure and nozzle internal flow field. The results of the three-dimensional flow analysis are in good agreement with available test data, and constitute the first rigorous numerical solution for canted nozzle flows since the inception of the Titan solid rocket motor program more than 25 years ago.				
20 DISTRIBUTION / AVAILABILITY OF ABSTRACT <input checked="" type="checkbox"/> UNCLASSIFIED/UNLIMITED <input type="checkbox"/> SAME AS RPT <input type="checkbox"/> DTIC USERS			21 ABSTRACT SECURITY CLASSIFICATION Unclassified	
22a NAME OF RESPONSIBLE INDIVIDUAL			22b TELEPHONE (Include Area Code)	22c OFFICE SYMBOL

DD FORM 1473, 84 MAR

83 APR edition may be used until exhausted
All other editions are obsolete.SECURITY CLASSIFICATION OF THIS PAGE
UNCLASSIFIED

NOMENCLATURE

a	exponent in the viscosity-temperature equation, (7)
\bar{A}	area used in Eq. (15)
A_j	dimensionless friction term defined in Eq. (2)
B_j	dimensionless energy exchange term defined in Eq. (3)
C_D	particle drag coefficient
\bar{C}_j	particle heat capacity
\bar{C}_p	gas specific heat at constant pressure
$\vec{D}, \vec{E}, \vec{F}, \vec{G}, \vec{H}$	vectors defined in Eq. (1)
D, E, F, G, H	vectors defined in Eq. (8)
e	dimensionless gas total energy per unit volume
f_j	momentum transfer parameter defined in Eq. (4)
g_c, g_r	convective and radiative parameters defined in Eq. (3)
h_j	dimensionless particle total energy per unit volume
\bar{L}	reference length scale, e.g., unit foot (ft) or unit meter (m)
M	gas-phase Mach number
\bar{m}_j	particle mass density
N	index: N = 1, one-phase flow; N = 2, two-phase flow
Nu_j	particle Nusselt number
p	dimensionless pressure
P_r	gas-phase Prandtl number
q, q_j	dimensionless gas; particle speed
\bar{r}_j	particle radius
R_w	dimensionless nozzle wall radial coordinate
Re_j	particle Reynolds number
\bar{t}	time, sec
t	dimensionless time, $t = \bar{v}_{max1} \bar{t} / \bar{L}$
T, T_j	dimensionless gas; particle temperature
u, v, w	dimensionless gas-phase velocity component along x, r, θ directions, respectively
u_j, v_j, w_j	dimensionless particle-phase velocity component along x, r, θ directions, respectively
\bar{v}_{max1}	adiabatic maximum speed evaluated at the inlet plane
\dot{w}	dimensionless mass flow rate defined in Eq. (15)

Accession For	
NTIS CRA&I	<input checked="" type="checkbox"/>
DTIC TAB	<input type="checkbox"/>
Unannounced	<input type="checkbox"/>
Justification _____	
By _____	
Distribution / _____	
Availability Codes	
Dist	<div style="display: flex; align-items: center;"> <div style="border: 1px solid black; padding: 2px; margin-right: 5px;">A-1</div> <div style="border: 1px solid black; padding: 2px; flex-grow: 1;"> <div style="display: flex; justify-content: space-between;"> ▲ □ </div> </div> </div>



NOMENCLATURE (Continued)

x, r, θ	dimensionless cylindrical coordinates
x, y, z	dimensionless rectangular coordinates
α_{ij}	direction cosines defined in Eq. (12)
β	nozzle canting angle
γ	gas specific heats ratio
δ	index: $\delta = 0$, rectangular coordinates; $\delta = 1$, cylindrical coordinates
ϵ, ϵ_j	gas accommodation coefficient and particle emissivity, respectively
ζ, ξ, η	transformed dimensionless coordinates
λ_q, λ_T	velocity lag, q_j/q ; temperature ratio, T/T_j
$\bar{\mu}$	micron, 10^{-6} m
$\bar{\mu}_g, \bar{\mu}_{t1}$	gas viscosity at local and stagnation state, respectively
π	3.1415926535898...
ρ, ρ_j	dimensionless gas; particle density
$\bar{\sigma}$	Stefan-Boltzmann constant
τ	$(\gamma-1)/(2\gamma)$
ϕ	particle mass fraction
ω	\bar{C}_j/\bar{C}_p

Superscript

\rightarrow	vectored quantity
$-$	dimensioned quantity

Subscript

g	gas-phase
j	particle-phase
$\max 1$	adiabatic maximum state evaluated at the inlet plane
$t1$	stagnation state evaluated at the inlet plane
1	motor coordinates
2	nozzle coordinates

CONTENTS

1. INTRODUCTION	7
2. GOVERNING EQUATIONS	11
3. THREE-DIMENSIONAL TRANSFORMATIONS	15
4. CONSIDERATION OF NOZZLE CANTING	17
5. SOLUTION METHOD	19
6. THREE-DIMENSIONAL BODY-FITTED GRIDS	27
7. ONE-PHASE COLD FLOW, $\gamma = 1.4$	31
8. ONE-PHASE HOT FLOW, $\gamma = 1.19$	37
9. TWO-PHASE HOT FLOW, GAS $\gamma = 1.19$	39
10. CONCLUSIONS	55
REFERENCES	57

FIGURES

1. Titan IV Motor Assembly and Launch Vehicle Configuration	8
2. Titan IV Motor Components	9
3. Titan IV Motor Aft Closure and Nozzle Configuration on the Symmetry Plane	9
4. Three-Dimensional Body-Fitted Coordinates Transformation	15
5. Determination of Flow Variables at Interface	23
6. Boundary Grids on Motor Entrance, Motor Symmetry, Nozzle Symmetry, and Nozzle Exit Planes	27
7. Three-Dimensional Body-Fitted Coordinates Grids for Motor and Nozzle	29
8. Motor and Nozzle Wall Geometry	29
9. Non-uniform Inflow at Motor Inlet Symmetric Plane (cold flow test data, $\gamma = 1.4$, Ref. 18)	32
10. Throat M and \dot{W} at Every Integration Step (one-phase, $\gamma = 1.4$)	32
11. Gas Mach Number Distribution (one-phase, $\gamma = 1.4$)	34
12. Mach Number Contour on Symmetry Plane (one-phase, $\gamma = 1.4$)	35
13. Three-Dimensional Mach Number Contour (one-phase, $\gamma = 1.4$)	35
14. Three-Dimensional Mach Number Contour (one-phase, $\gamma = 1.19$)	38
15. Mach Number Contour on Symmetry Plane (two-phase, $\gamma = 1.19$)	40
16. Three-Dimensional Mach Number Contour (two-phase, $\gamma = 1.19$)	40
17. Comparison of Mach Number Distributions (motor)	41
18. Comparison of Mach Number Distributions (nozzle)	42
19. Comparison of Pressure Distributions (motor)	42
20. Comparison of Pressure Distributions (nozzle)	43
21. Gas Velocity Vectors on Symmetry Plane (two-phase, $\gamma = 1.19$)	44
22. Three-Dimensional Gas Velocity Vectors (two-phase, $\gamma = 1.19$)	45

FIGURES (Continued)

23.	Particle Density Contour on Symmetry Plane (two-phase, $\gamma = 1.19$)	46
24.	Three-Dimensional Particle Density Contour (two-phase, $\gamma = 1.19$)	46
25.	Particle Velocity Vectors on Symmetry Plane (two-phase, $\gamma = 1.19$)	47
26.	Three-Dimensional Particle Velocity Vectors (two-phase, $\gamma = 1.19$)	47
27.	Particle Velocity Lag and Temperature Ratio (nozzle)	48
28.	Three-Dimensional Mach Number Contour, Titan IV Solid Rocket Motor (one-phase flow, $\gamma = 1.19$)	50
29.	Three-Dimensional Mach Number Contour, Titan IV Solid Rocket Motor (two-phase flow, $\gamma = 1.19$)	51
30.	Three-Dimensional Gas Pressure Contour, Titan IV Solid Rocket Motor (two-phase flow, $\gamma = 1.19$)	52
31.	Three-Dimensional Particle Density Contour, Titan IV Solid Rocket Motor (two-phase flow, $\gamma = 1.19$)	53

1. INTRODUCTION

Modern, advanced, complex defense technologies often require an unconventional design of propulsive devices which deviates greatly from an axisymmetric configuration. These unorthodox propulsion concepts carry design flexibility to a far more extensive domain of application and offer some special fluid dynamic advantages over those with a circular-shaped design. Typical examples of three-dimensional odd-shaped propulsive devices can be found in:

- The scramjet powered hypersonic aerospace plane, which uses part of the vehicle under-surface to provide additional flow expansion
- The F-18 Hornet fighter aircraft, which utilizes movable square-shaped exhaust ducts to obtain more lift and better maneuverability
- A new cruise-missile concept, which integrates a series of rectangular exhaust nozzles into the airframe for low observability
- A new aircraft concept, which features non-circular engines with a vectoring nozzle mounted in the wings for maximum propulsive lift
- The anti-satellite miniature vehicle, which adopts 64 circumferentially mounted square nozzles for enhanced trajectory control

More often, however, non-axisymmetric propulsive mechanizations for thrust vector control (TVC) are found in space launch vehicles; e.g., PAMD-II solid rocket motor (SRM) with swivel ball joint, Inertial Upper Stage (IUS) SRMs with fluid bearing, Minuteman III first stage with swivel ball joint, and Space Shuttle SRM with flexible bearing. Another classic example of this category is the Titan III SRM with canted nozzle.

For many years, the Titan III 120-in. diameter, five-segment SRM (SRM1205) has been a very reliable booster for delivering large payloads into space for various missions. The motor consists of a forward closure, five cylindrical segments, aft closure with canted nozzle, exit cone, and exit cone extension. The nozzle is canted 6° from bottom dead center (BDC) toward top dead center

(TDC) to provide a thrust vector which intersects the central liquid-fueled core vehicle at its center of gravity. An enhanced version of the motor is the 5-1/2 segment motor (T34D SRM), which includes an additional half-cylindrical segment near the forward closure. The T34D SRM was first utilized in 1982 to successfully boost the IUS vehicle and spacecraft into low earth orbit; it has since replaced the SRM1205 as zero stage Titan III during launching of large spacecraft into orbit. More recently, a seven-segment Titan IV SRM is being developed to meet an ever increasing payload demand. This is an improved version of the seven-segment motor (SRM1207) statically tested in 1969 for the Manned Orbiting Laboratory (MOL) program. In the wake of the tragic failure of the Space Shuttle Challenger on 28 January 1986, the Titan IV SRM has an even greater role than that originally perceived in the expendable launch vehicle program for unmanned flight missions. Figure 1 shows the Titan IV motor assembly and launch vehicle configuration. Figure 2 shows the Titan IV SRM components. Figure 3 illustrates the non-axisymmetric motor aft closure geometry and canted nozzle design.

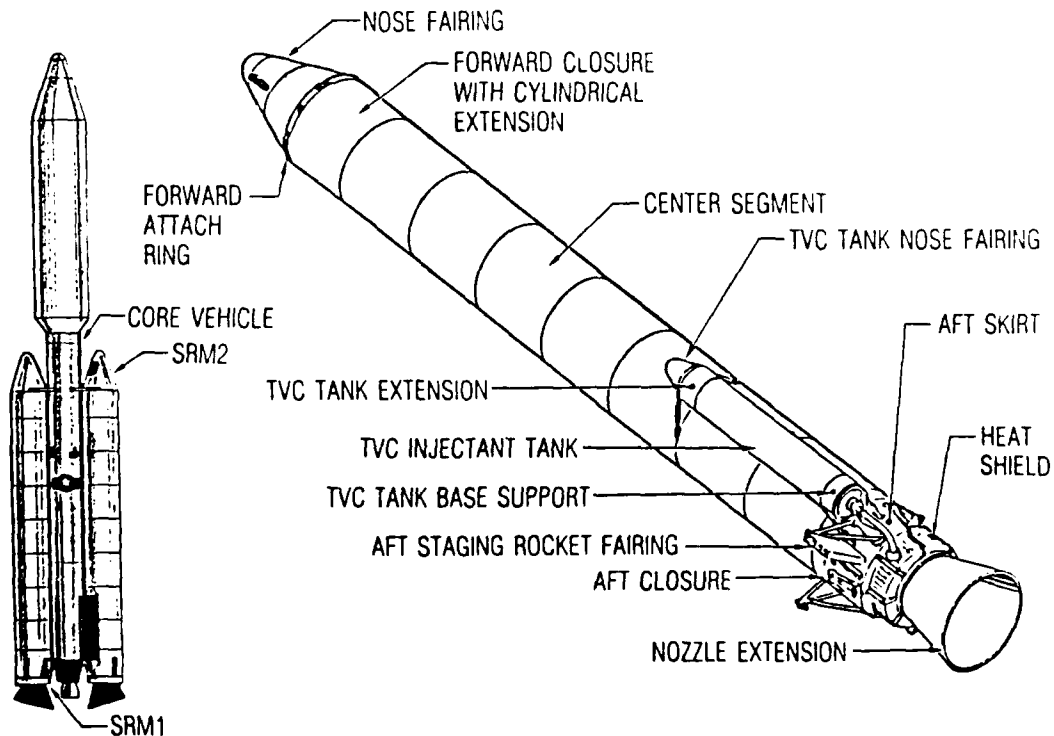


Figure 1. Titan IV Motor Assembly and Launch Vehicle Configuration

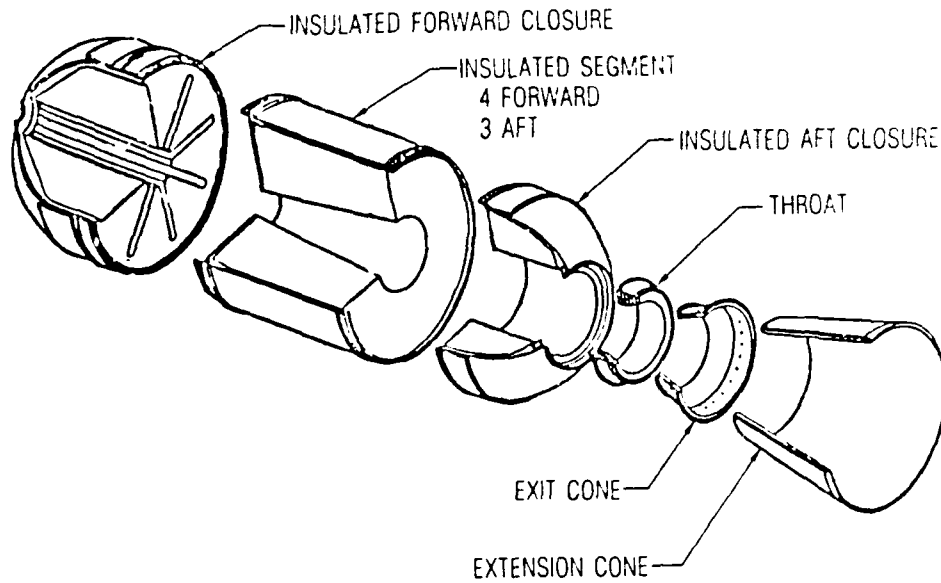


Figure 2. Titan IV Motor Components

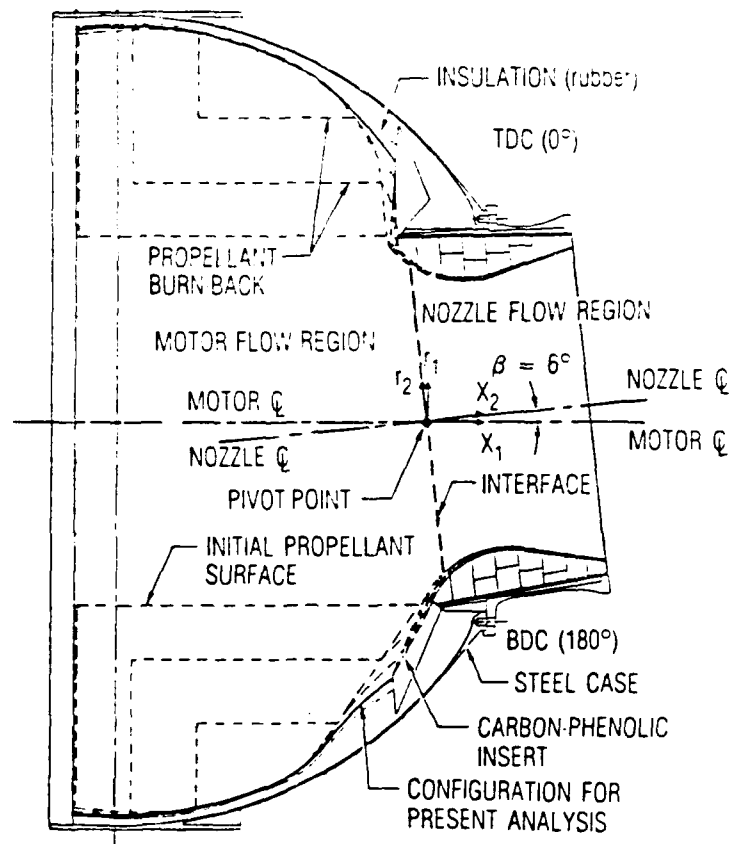


Figure 3. Titan IV Motor Aft Closure and Nozzle Configuration on the Symmetry Plane

As a result of the wide application of asymmetric nozzle configurations in industry, three-dimensional nozzle analysis has received great attention. Reference 1 lists some recent developments in this area for gas-only, one-phase flows inside three-dimensional nozzles. Gas-particle, two-phase flows inside rocket nozzles were studied in References 2 through 7 in one-dimensional or two-dimensional spaces. Reference 8 solved three-dimensional, two-phase flows inside the supersonic portion of nozzles. However, a comprehensive gas-particle, two-phase, subsonic-transonic flow inside a three-dimensional canted nozzle has yet to be addressed in literature. In fact, for more than a quarter century since the inception of the Titan solid rocket motor program, a detailed solution of two-phase, subsonic-transonic flows inside the canted Titan SRM nozzle has yet to be obtained. The transonic flow solution is recognized in industry as a bottleneck in many three-dimensional nozzle flow studies including all of the unorthodox propulsive devices mentioned before.

In this report, a time-dependent numerical scheme (which has been used successfully in Reference 7 for axisymmetric/two-dimensional solutions), in conjunction with the three-dimensional, body-fitted, coordinate transformation technique of References 9 and 10, is utilized for the solution of both gas-only, one-phase and fully coupled gas-particle, two-phase subsonic-transonic-supersonic flows inside three-dimensional nozzles of arbitrary configurations. Detailed results of the calculation are presented for the Titan IV canted nozzle flow, even though the computer program, which has been developed under this study, is equally applicable to other odd-shaped, three-dimensional nozzle configurations. The computation from the present time-dependent scheme is carried out to a low supersonic nozzle exit plane. Further expansion of the flow in the downstream direction can be evaluated from an efficient steady-state, forward marching scheme presented in Reference 8.

2. GOVERNING EQUATIONS

Normalized by the gas-phase stagnation state corresponding to the condition at the inlet plane, the governing equations written in weak conservative form for an unsteady, three-dimensional, two-phase flow are

$$\frac{\partial \tilde{D}}{\partial t} + \frac{\partial \tilde{E}}{\partial x} + \frac{\partial \tilde{F}}{\partial r} + \frac{\partial \tilde{G}}{\partial \theta} + \tilde{H} = 0 \quad (1)$$

$$\tilde{D} = \begin{bmatrix} \rho \\ \rho u \\ \rho v \\ \rho w \\ e \\ \rho_j(N-1) \\ \rho_j u_j(N-1) \\ \rho_j v_j(N-1) \\ \rho_j w_j(N-1) \\ h_j(N-1) \end{bmatrix}; \quad \tilde{E} = \begin{bmatrix} \rho u \\ \tau_p + \rho u^2 \\ \rho uv \\ \rho uw \\ [e + (\gamma - 1)p] u \\ \rho_j u_j(N-1) \\ \rho_j u_j^2(N-1) \\ \rho_j u_j v_j(N-1) \\ \rho_j u_j w_j(N-1) \\ h_j u_j(N-1) \end{bmatrix}; \quad \tilde{F} = \begin{bmatrix} \rho v \\ \rho uv \\ \tau_p + \rho v^2 \\ \rho vw \\ [e + (\gamma - 1)p] v \\ \rho_j v_j(N-1) \\ \rho_j u_j v_j(N-1) \\ \rho_j v_j^2(N-1) \\ \rho_j v_j w_j(N-1) \\ h_j v_j(N-1) \end{bmatrix}$$

$$\tilde{G} = \frac{1}{r\delta} \begin{bmatrix} \rho w \\ \rho uw \\ \rho vw \\ \tau_p + \rho w^2 \\ [e + (\gamma - 1)p] w \\ \rho_j w_j(N-1) \\ \rho_j u_j w_j(N-1) \\ \rho_j v_j w_j(N-1) \\ \rho_j w_j^2(N-1) \\ h_j w_j(N-1) \end{bmatrix}; \quad \tilde{H} = \frac{\delta}{r\delta} \begin{bmatrix} \rho v \\ \rho uv \\ \rho(v^2 - w^2) \\ 2\rho vw \\ [e + (\gamma - 1)p] v \\ \rho_j v_j(N-1) \\ \rho_j u_j v_j(N-1) \\ \rho_j(v_j^2 - w_j^2)(N-1) \\ 2\rho_j v_j w_j(N-1) \\ h_j v_j(N-1) \end{bmatrix} + (N-1)\rho_j \begin{bmatrix} A_j \\ B_j \\ 0 \\ -(u - u_j) \\ -(v - v_j) \\ -(w - w_j) \\ -B_j \end{bmatrix}$$

with friction term

$$A_j = \frac{9}{2} \frac{\bar{\mu}_j f_j}{\bar{m}_j \bar{r}_j^2} \frac{\bar{L}}{\bar{V}_{max1}} \quad (2)$$

and energy exchange term

$$B_j = 2\gamma[\vec{q}_j \cdot \Delta\vec{q}_j - g_c(T_j - T) - g_r(\epsilon_j T_j^4 - \epsilon T^4)] \quad (3)$$

where

$$g_c = Nu_j / (6 f_j P_r), \quad g_r = \bar{\sigma} \bar{r}_j \bar{T}_{tl}^3 / (3 \bar{c}_p \bar{\mu}_j f_j)$$

$$\vec{q}_j \cdot \Delta\vec{q}_j = u_j(u - u_j) + v_j(v - v_j) + w_j(w - w_j)$$

$$T = \frac{P}{\rho}; \quad T_j = [h_j / \gamma \rho_j - (u_j^2 + v_j^2 + w_j^2)] / \omega$$

The momentum transfer parameter f_j is defined as

$$f_j = C_D / C_{D_{Stokes}} \quad (4)$$

where C_D is the particle drag coefficient given in Reference 11 and $C_{D_{Stokes}} = 24 / Re_j$.

The heat transfer parameter, namely the particle Nusselt number, is taken as (Ref. 12)

$$Nu_j = 2 + 0.459 Re_j^{0.55} P_r^{0.33} \quad (5)$$

The particle Reynolds number is based on relative speed

$$|\Delta\vec{q}_j| = \sqrt{(u - u_j)^2 + (v - v_j)^2 + (w - w_j)^2}$$

and is defined as follows:

$$Re_j = \frac{2 \left| \Delta \bar{q}_j \right| \bar{r}_j \bar{\rho}}{\bar{\mu}_g} = 2 \left| \Delta q_j \right| \rho \frac{\bar{r}_j}{\bar{\mu}_g} \frac{1}{\tau} \frac{\bar{p}_{t1}}{\bar{V}_{max1}} \quad (6)$$

The gas viscosity is evaluated from

$$\bar{\mu}_g = \bar{\mu}_{ti} (\bar{T}/\bar{T}_{ti})^a \quad (7)$$

3. THREE-DIMENSIONAL TRANSFORMATIONS

From a general, three-dimensional, arbitrary configuration in the physical region (x,y,z) , the one-to-one differentiable transformation to a rectangular grid with a uniform square mesh in the computational domain (ζ, ξ, η) shown in Figure 4 can be accomplished by using a three-dimensional, body-fitted, coordinate system developed in References 9 and 10. This system requires the solution of three quasi-linear, elliptic, partial differential equations (PDE) with Dirichlet boundary conditions. The method which utilizes a successive over-relaxation technique to solve the quasi-linear elliptic PDEs and to generate a body-fitted coordinate system is discussed in detail in References 9 and 10.

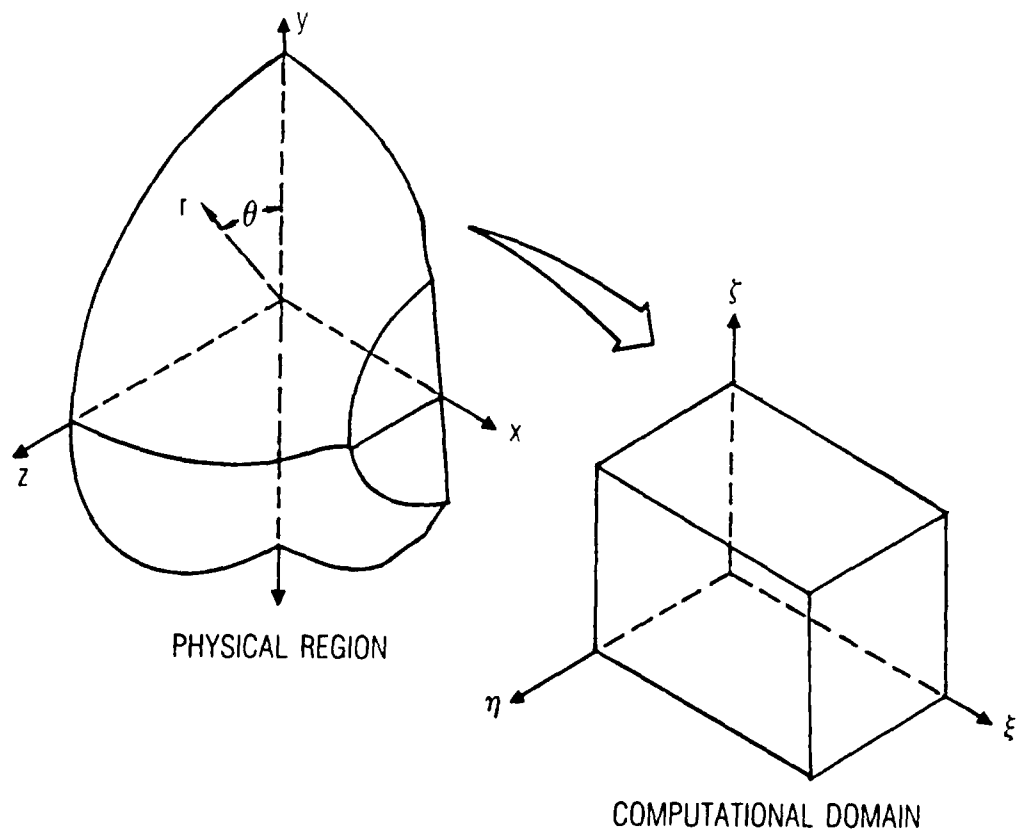


Figure 4. Three-Dimensional Body-Fitted Coordinates Transformation

Formally applying the chain rule of change of independent variables for Eq. (1) results in the following conservation laws in the (ζ, ξ, η) space:

$$\frac{\partial D}{\partial t} + \frac{\partial E}{\partial \zeta} + \frac{\partial F}{\partial \xi} + \frac{\partial G}{\partial \eta} + H = 0 \quad (8)$$

with

$$\begin{aligned} D &= J_2 \tilde{D} \\ E &= C_{11} \tilde{E} + C_{12} \tilde{F} + C_{13} \tilde{G} \\ F &= C_{21} \tilde{E} + C_{22} \tilde{F} + C_{23} \tilde{G} \\ G &= C_{31} \tilde{E} + C_{32} \tilde{F} + C_{33} \tilde{G} \\ H &= J_2 \tilde{H} \end{aligned}$$

where the scale factors

$$\begin{aligned} C_{11} &= y_{\xi} z_{\eta} - y_{\eta} z_{\xi}, & C_{12} &= x_{\eta} z_{\xi} - x_{\xi} z_{\eta}, & C_{13} &= x_{\xi} y_{\eta} - x_{\eta} y_{\xi} \\ C_{21} &= y_{\eta} z_{\zeta} - y_{\zeta} z_{\eta}, & C_{22} &= x_{\zeta} z_{\eta} - x_{\eta} z_{\zeta}, & C_{23} &= x_{\eta} y_{\zeta} - x_{\zeta} y_{\eta} \\ C_{31} &= y_{\zeta} z_{\xi} - y_{\xi} z_{\zeta}, & C_{32} &= x_{\xi} z_{\zeta} - x_{\zeta} z_{\xi}, & C_{33} &= x_{\zeta} y_{\xi} - x_{\xi} y_{\zeta} \end{aligned}$$

and the Jacobian of transformation

$$J_2 = \begin{vmatrix} x_{\xi} & x_{\eta} & x_{\zeta} \\ y_{\xi} & y_{\eta} & y_{\zeta} \\ z_{\xi} & z_{\eta} & z_{\zeta} \end{vmatrix} \quad (9)$$

are evaluated from numerical differentiation of the converged solution of the body-fitted coordinate system. Note that use of the Jacobian in a multi-dimensional transformation (Ref. 13) eliminates the need to evaluate second-order partial derivatives for the scale factors of transformation. In the physical region described by the cylindrical coordinate system (x, r, θ) , the independent variable y is replaced by r ; z is replaced by θ in the scale factors and the Jacobian of transformation.

4. CONSIDERATION OF NOZZLE CANTING

The geometric transformation mentioned before is applicable to a wide range of irregular, three-dimensional configurations with the same set of coordinate systems for the motor chamber (hereafter referenced as "motor") and the nozzle. However, an added difficulty arises when the nozzle is canted or gimballed, thereby creating a different reference coordinate system for the nozzle from that for the motor. In a canted nozzle flow, the nozzle coordinate centerline is rotated an angle β from that of the motor centerline as shown in Figure 3 for a Titan IV SRM aft closure configuration. Use of either the motor centerline or the nozzle centerline as a fixed reference coordinate centerline for the entire flow field is incorrect. Ambiguous interpretation of flow data ensues when only one set of the fixed reference coordinate systems is adopted. In this regard, it is obvious that a one-dimensional analysis--based on an average area approach--or a two-dimensional study--based on a simplified, axisymmetric geometry--will produce results of questionable value to a three-dimensional, canted nozzle flow investigation.

In this study, separate coordinate systems are used for the motor and nozzle flow regions. Two separate three-dimensional, body-fitted, coordinate systems utilizing the transformation technique mentioned above are generated for the motor and the nozzle. The interface between the two flow regions is taken to be a plane passing through the pivot point of canting and perpendicular to the nozzle centerline as shown in Figure 3. The flows in the two regions are solved simultaneously. The treatment of flow variables at the interface needs special attention and is discussed later. In this way, confusion is eliminated as to the use of the motor or nozzle centerline as a reference coordinate centerline for a canted nozzle flow field. Precise interpretation of flow data can be obtained. This concept of multiple grids for a canted nozzle flow can be extended to a three-dimensional, compressible flow inside a curved passage.

5. SOLUTION METHOD

The weak conservative formulation [Eq. (8)] is a hyperbolic type with respect to the time variable in subsonic, transonic, and supersonic flows; it can be solved with the MacCormack finite difference scheme (Ref. 14) which has been used successfully for the asymptotic solution of time-dependent, axisymmetric/two-dimensional, two-phase nozzle flows (Ref. 7) and the steady-state solution of three-dimensional, two-phase supersonic nozzle flows (Ref. 8). In the present study, the initial condition for one-phase flow is based on a one-dimensional isentropic assumption, with the flow vector set to a local inclination angle from linear interpolation between the lower and upper wall along the same grid line (constant ζ , η line). The converged, one-phase results serve as an initial guess for the gas-phase in the gas-particle two-phase flow. Zero lag ($\lambda_q = \lambda_T = 1$) between the particle and gas phase is assumed initially to start the two-phase flow calculation. This calculation procedure and the inclusion of fourth-order damping terms to the second-order MacCormack finite difference scheme are much the same as those in Reference 1, except with an added dimension along the circumferential direction.

The nozzle exit boundary condition is based on a linear extrapolation of conservative variables [\tilde{D} of Eq. (1)], since the flow is assumed to be supersonic at the nozzle exit plane, and any error generated from the extrapolation is not expected to propagate back and affect upstream results.

Two choices of inlet boundary conditions applied to the motor entrance region have been incorporated into the computer program. The first inlet boundary condition is obtained from an axisymmetric characteristics formulation similar to that discussed in Reference 15 and used in Reference 7. This boundary condition applies to an axisymmetric inlet flow but can be extended to non-axisymmetric, three-dimensional inlet flow (Ref. 16). The solution obtained from applying this inlet boundary condition usually converges to a fairly smooth, low subsonic inlet condition close to an isentropic, uniform, one-dimensional inlet flow; it is suitable for the inlet flow that is not perturbed significantly by crossflow occurring upstream of the inlet plane.

The second inlet boundary condition corresponds to specified fixed flow variables at the inlet plane. For one-phase flow, Mach number, flow angles, and static pressure are specified on the inlet plane. For two-phase flow, particle velocity lag (λ_q) and gas-to-particle temperature ratio (λ_T) are also needed on the inlet plane. This inlet boundary condition is suitable for a non-uniform flow at the inlet plane, where flow variables can be obtained from experimental data or theoretical analysis. In applying this inlet boundary condition, a second order interpolation along the axial main flow direction is desirable to smooth the flow variables at the grid points adjacent to the inlet plane in order to avoid instability near the motor inlet region.

For a cylindrical coordinate system, the conservative variables \tilde{G} and \tilde{H} in Eq. (1) at motor and nozzle centerlines are obtained from a linear extrapolation of the values at the interior points. In decoding conservative variable, \tilde{D} , the flow variables at the motor and nozzle centerlines are obtained from interpolating the flow variables at one grid point above and at one grid point below the centerline on the symmetry plane. In a non-axisymmetric nozzle, the radial velocity components at the coordinate centerline are not necessarily zero. On the symmetry plane, however, the meridional velocity components are zero. Therefore, at $\theta = 0$ on the symmetry plane, the following relations are used:

$$f_{1,1} = f_{2,1} - (f_{2,1} - f_{2,NK}) \frac{r_{2,1}}{(r_{2,1} + r_{2,NK})}$$

where $f_{j,k}$ stands for ρ , u , e , ρ_j , u_j , and h_j , and the subscripts indicate grid point indexes along r , θ directions on a constant ζ plane;

$$g_{1,1} = g_{2,1} - (g_{2,1} + g_{2,NK}) \frac{r_{2,1}}{(r_{2,1} + r_{2,NK})}$$

where $g_{j,k}$ stands for v and v_j ; and

$$h_{1,1} = 0$$

where $h_{j,k}$ stands for w and w_j .

The scalar flow variables and velocity vectors are uniquely defined at the coordinate centerlines from the equations previously shown. The components of the velocity vector, however, take different values at different meridional planes. Therefore, at $\theta \neq 0$ on the symmetry plane centerlines, the flow variables are computed from those at $\theta = 0$ as follows:

$$f_{1,k} = f_{1,1}$$

$$g_{1,k} = g_{1,1} \cos \theta + h_{1,1} \sin \theta$$

$$h_{1,k} = -g_{1,1} \sin \theta + h_{1,1} \cos \theta$$

In this way, the flow variables at the coordinate centerlines of the motor and nozzle in cylindrical coordinates are evaluated in a three-dimensional fashion without ambiguity and undue complication.

The flow variables at the wall boundary are obtained from linear extrapolation of data from the adjacent interior points and then modified by the local tangency condition, $\vec{q} \cdot \vec{n}_w = 0$, with three components of velocity vector found as follows:

$$u = |\vec{q}| \vec{n}_t \cdot \vec{i}_x$$

$$v = |\vec{q}| \vec{n}_t \cdot \vec{i}_r$$

$$w = |\vec{q}| \vec{n}_t \cdot \vec{i}_\theta$$

where \vec{q} is the gas velocity vector on the wall and $\vec{i}_x, \vec{i}_r, \vec{i}_\theta$ are the unit vectors in x, r, θ , directions, respectively.

$$\vec{n}_t = \frac{\vec{q} - (\vec{q} \cdot \vec{n}_w) \vec{n}_w}{|\vec{q} - (\vec{q} \cdot \vec{n}_w) \vec{n}_w|}$$

is the unit tangent vector on the wall and

$$\vec{n}_w = \frac{-\nabla f}{|\nabla f|} = \frac{-\vec{i}_r + \frac{\partial R_w}{\partial x} \vec{i}_x + \frac{\partial R_w}{R_w \partial \theta} \vec{i}_\theta}{\sqrt{1 + \left(\frac{\partial R_w}{\partial x}\right)^2 + \left(\frac{\partial R_w}{R_w \partial \theta}\right)^2}}$$

is the unit normal vector to the wall for $[f(x, r, \theta)]_w = [r - R_w(x, \theta)] = 0$ in a cylindrical coordinate system or

$$\vec{n}_w = \frac{f_x \vec{i}_x + f_y \vec{i}_y + f_z \vec{i}_z}{\sqrt{f_x^2 + f_y^2 + f_z^2}}$$

for $[f(x, y, z)]_w = 0$ in a rectangular coordinate system. Similar expressions are applied to the particle-phase velocity components, even though it is recognized that particles would interact with the solid wall in a complicated manner, which accounts for enhanced motor and nozzle wall erosion. The particle-boundary interaction is a subject of further research.

On the interface plane of the motor and nozzle flow regions, the flow variables are evaluated from interpolating variables at upstream and downstream nodal points on the motor and nozzle interface, respectively, as illustrated in Figure 5. The scalar flow variables (pressure, density, temperature, and total energy) on the interface plane are invariant with respect to coordinate change from the motor to nozzle centerline and can be obtained directly from this interpolation process. The velocity vector, however, has different components on the interface for the motor and nozzle, respectively, and can be found by the following method.

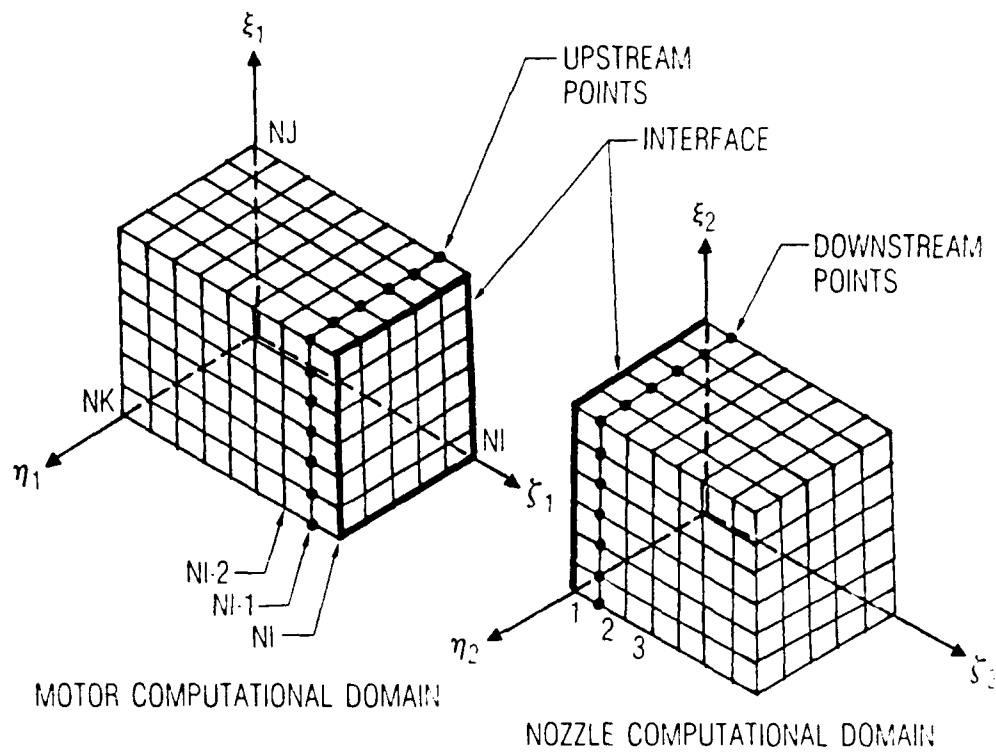


Figure 5. Determination of Flow Variables at Interface

Let the velocity at any point in the motor coordinates be

$$\vec{q} = u_1 \vec{i}_{x1} + v_1 \vec{i}_{r1} + w_1 \vec{i}_{\theta1}$$

where \vec{i}_{x1} , \vec{i}_{r1} , $\vec{i}_{\theta1}$ are the unit vectors in the motor coordinates. This same vector at the same point in the nozzle coordinates is

$$\vec{q} = u_2 \vec{i}_{x2} + v_2 \vec{i}_{r2} + w_2 \vec{i}_{\theta2}$$

where \vec{i}_{x2} , \vec{i}_{r2} , $\vec{i}_{\theta2}$ are the unit vectors in the nozzle coordinates.

Since both the motor and nozzle coordinates are orthogonal, the dot products

$$\vec{i}_{x1} \cdot \vec{q}, \vec{i}_{r1} \cdot \vec{q}, \text{ and } \vec{i}_{\theta1} \cdot \vec{q}$$

give

$$\begin{aligned}
 u_1 &= \alpha_{11}u_2 + \alpha_{12}v_2 + \alpha_{13}w_2 \\
 v_1 &= \alpha_{21}u_2 + \alpha_{22}v_2 + \alpha_{23}w_2 \\
 w_1 &= \alpha_{31}u_2 + \alpha_{32}v_2 + \alpha_{33}w_2
 \end{aligned} \tag{10}$$

where $\alpha_{11} = \vec{i}_{x1} \cdot \vec{i}_{x2}$, $\alpha_{12} = \vec{i}_{x1} \cdot \vec{i}_{r2}$, $\alpha_{13} = \vec{i}_{x1} \cdot \vec{i}_{\theta2}$ and so forth are the direction cosines. Similarly

$$\begin{aligned}
 u_2 &= \alpha_{11}u_1 + \alpha_{21}v_1 + \alpha_{31}w_1 \\
 v_2 &= \alpha_{12}u_1 + \alpha_{22}v_1 + \alpha_{32}w_1 \\
 w_2 &= \alpha_{13}u_1 + \alpha_{23}v_1 + \alpha_{33}w_1
 \end{aligned} \tag{11}$$

Note $\sum_{j=1}^3 \alpha_{ij}\alpha_{kj} = \delta_{ik} =$ Kronecker delta function.

For a nozzle with canting angle β , the direction cosines are

$$\alpha_{ij} = \begin{vmatrix} \cos\beta & -\sin\beta\cos\theta_2 & \sin\beta\sin\theta_2 \\ \sin\beta\cos\theta_1 & \cos\beta\cos\theta_1\cos\theta_2 + \sin\theta_1\sin\theta_2 & -\cos\beta\cos\theta_1\sin\theta_2 + \sin\theta_1\cos\theta_2 \\ -\sin\beta\sin\theta_1 & -\cos\beta\sin\theta_1\cos\theta_2 + \cos\theta_1\sin\theta_2 & \cos\beta\sin\theta_1\sin\theta_2 + \cos\theta_1\cos\theta_2 \end{vmatrix} \tag{12}$$

and the two coordinates are related by the following equations:

$$\tan\theta_1 = \frac{r_2 \sin\theta_2}{x_2 \sin\beta + r_2 \cos\beta \cos\theta_2}$$

$$r_1 = \frac{x_2 \sin\beta + r_2 \cos\beta \cos\theta_2}{\cos\theta_1} = \frac{r_2 \sin\theta_2}{\sin\theta_1} \quad (13)$$

$$x_1 = x_2 \cos\beta - r_2 \sin\beta \cos\theta_2$$

$$\tan\theta_2 = -\frac{r_1 \sin\theta_1}{-x_1 \sin\beta + r_1 \cos\beta \cos\theta_1}$$

$$r_2 = \frac{-x_1 \sin\beta + r_1 \cos\beta \cos\theta_1}{\cos\theta_2} = \frac{r_1 \sin\theta_1}{\sin\theta_2} \quad (14)$$

$$x_2 = x_1 \cos\beta + r_1 \sin\beta \cos\theta_1$$

which also imply that uniform circumferential grid division in θ_2 (nozzle coordinates) will result in non-uniform circumferential grid division in θ_1 (motor coordinates) on the interface plane for a nozzle with non-zero canting angle.

Equation (10) is used to define the components of velocity vectors on the nozzle side with respect to the motor coordinates, and Equation (11) is used to define the components of velocity vectors on the motor side with respect to the nozzle coordinates. The velocity components at the interface are found from interpolating the velocity components at the upstream and downstream grid points adjacent to the interface with a consistent reference (motor or nozzle) coordinate system.

6. THREE-DIMENSIONAL BODY-FITTED GRIDS

The initial guess of three-dimensional body-fitted grids for both motor and nozzle are based on linear interpolation from a specified boundary nodal points arrangement, which consists of: (a) the two-dimensional boundary-fitted-coordinate systems (Ref. 17) in upper (TDC, $\theta = 0$) and lower (BDC, $\theta = \pi$) symmetry planes and at 90° ($\theta = \pi/2$) plane for both motor and nozzle flow regions; (b) a uniform circumferential division for nozzle and a non-uniform circumferential division for motor according to Eqs. (13) and (14); and (c) the linearly interpolated grid radial coordinates between TDC and 90° and between 90° and BDC for motor inlet, interface, and nozzle exit planes. Care has been taken to ensure that grid points are continuous on the coordinate centerlines and on the interface plane that joins the motor and nozzle flow regions. These boundary nodal meshes are presented in Figure 6 for the Titan IV motor and nozzle configuration shown in Figure 3 when the aft closure propellant is completely consumed, corresponding to a time approximately 78.5 sec into motor burn for a nominal motor burn time of 123 sec.

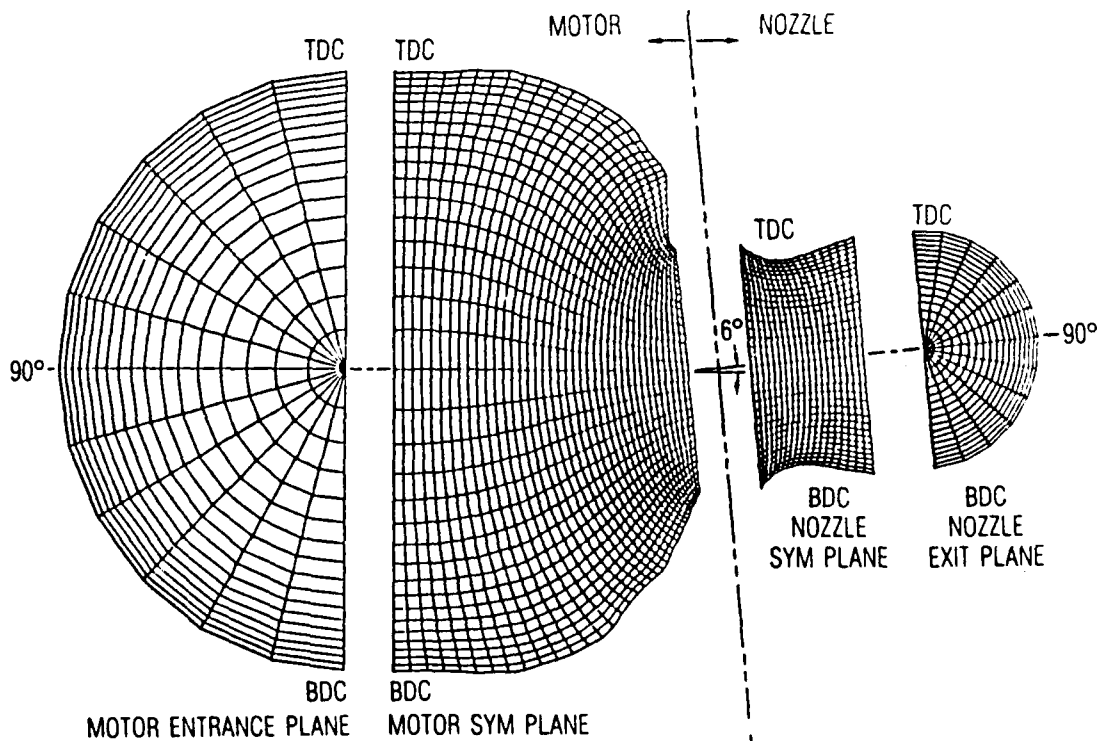


Figure 6. Boundary Grids on Motor Entrance, Motor Symmetry, Nozzle Symmetry, and Nozzle Exit Planes

The inhomogeneous terms in the boundary-fitted coordinate transformation have been turned on to keep the streamwise grid lines near the nozzle wall in the concave region. For irregular motor and nozzle configurations whose boundary geometry cannot be satisfactorily described by linear interpolation of radial coordinates between TDC and 90° , and between 90° and BDC planes, provisions have been incorporated in the program to allow for geometry input of boundary radial coordinates on any specified meridional planes in addition to those at TDC, 90° and BDC.

The three-dimensional interior grid points are generated from a successive over-relaxation iteration scheme for the solution of the three-dimensional quasi-linear elliptic system mentioned before. With the careful arrangement of boundary nodal meshes, fast convergence of iteration for the three-dimensional interior grid generation is assured. It is important that the inhomogeneous terms in the three-dimensional body-fitted coordinate system for the interior nodal points generation be included, to be compatible with the two-dimensional boundary-fitted coordinates specified on the three-dimensional grid boundaries for nodal points clustering control. An exponential decay function, similar to that in Reference 17, is applied for the three-dimensional interior coordinate control. It takes 17.2 sec to generate a three-dimensional Titan IV motor grid ($N_I = 40$, $N_J = 18$, $N_K = 13$ in the x , r , θ directions, respectively) and 1.2 sec to generate a Titan IV SRM three-dimensional nozzle grid ($20 \times 18 \times 13$) on a CRAY X-MP14 super computer. Numerical differentiation is then utilized to calculate the scale factors of transformation from an irregular three-dimensional physical region to a uniformly divided rectangular parallelepiped computational domain. This process takes only 0.1 sec for the motor and 0.01 sec for the nozzle flow region. The hidden-line plots of the converged Titan IV SRM three-dimensional grids are shown in Figure 7, and the wall boundary geometry for the motor and nozzle is given in Figure 8.

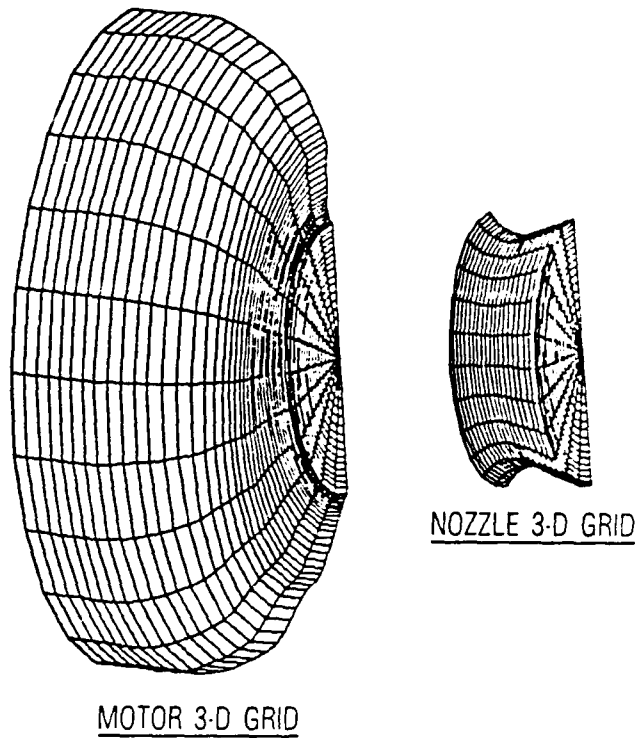


Figure 7. Three-Dimensional Body-Fitted Coordinates Grids for Motor and Nozzle

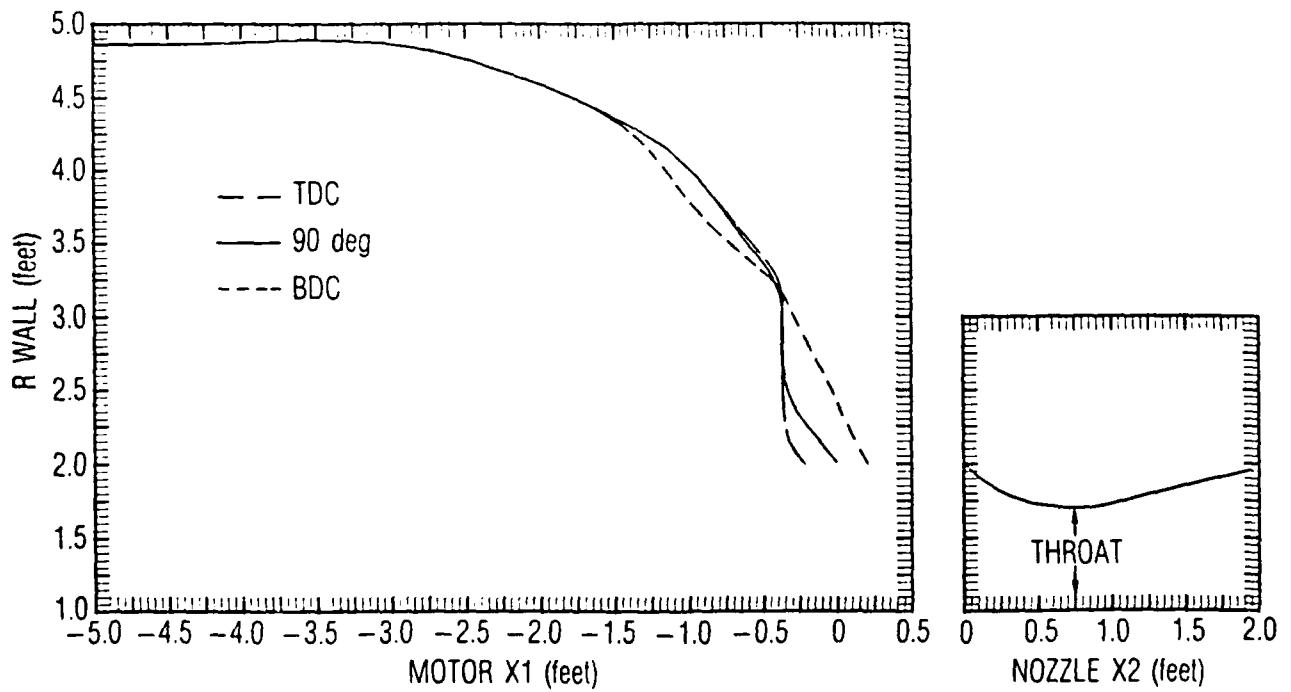


Figure 8. Motor and Nozzle Wall Geometry

7. ONE-PHASE COLD FLOW, $\gamma = 1.4$

To aid design and evaluation of the full-scale Titan IV SRM, a cold flow test with a 4.65% scale model was conducted (Ref. 18). Gaseous nitrogen ($\gamma = 1.4$) was introduced uniformly into the scaled motor chamber through sintered bronze porous surfaces to simulate propellant burning. Nitrogen was introduced at a chamber pressure of 45 psia and chamber temperature of 492°R. The model nozzle throat diameter was 1.895 in. An exact scale-down of the motor aft closure and nozzle configurations was utilized in the cold flow test. This model provided test data for comparison with results from the present theoretical calculation.

In the one-phase cold flow ($\gamma = 1.4$) numerical study, the fixed non-uniform inflow condition is taken from the three-dimensional cold flow test data at TDC and BDC planes as illustrated in Figure 9. An isentropic one-dimensional Mach number at the same area ratio is also indicated in the figure for comparison. Inflow Mach numbers at other meridional planes are obtained from linear interpolation of the Mach numbers at TDC and BDC planes. The computed dimensionless mass flow rate, wall Mach number at TDC, 90°, BDC, and centerline Mach number at the throat station for every integration step are shown in Figure 10. The initial throat centerline Mach number is less than one, because the grid plane (constant ζ plane) passing through the throat station at the nozzle wall is initially taken to be a sonic surface which curves toward downstream at the centerline in the physical region. This helps to speed up the solution convergence. Note that

$$\dot{W} = \iint (\bar{\rho}\bar{u} + \bar{\rho}_j\bar{u}_j) d\bar{A} / [(2\pi)^{\delta} \bar{\rho}_{t1} \bar{V}_{max1} \bar{L}^2] \quad (15)$$

is the dimensionless mass flow rate evaluated at the nozzle geometric throat. For a one-phase flow, the contribution from particle mass flux is zero.

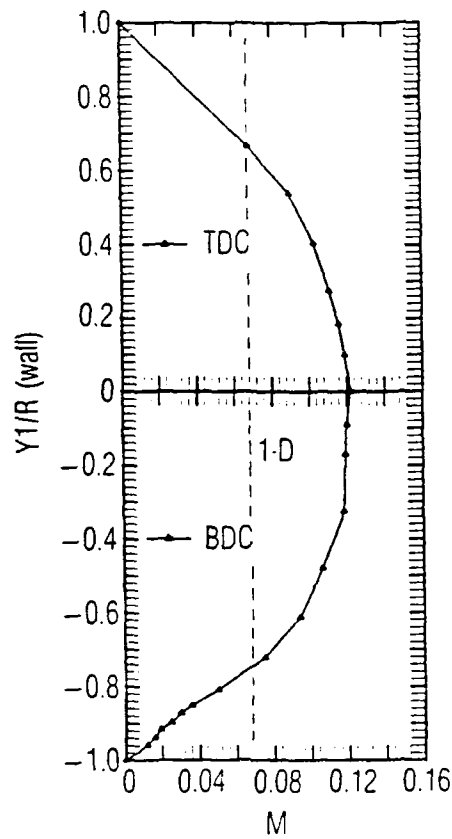


Figure 9. Non-uniform Inflow at Motor Inlet Symmetric Plane (cold flow test data, $\gamma = 1.4$, Ref. 18)

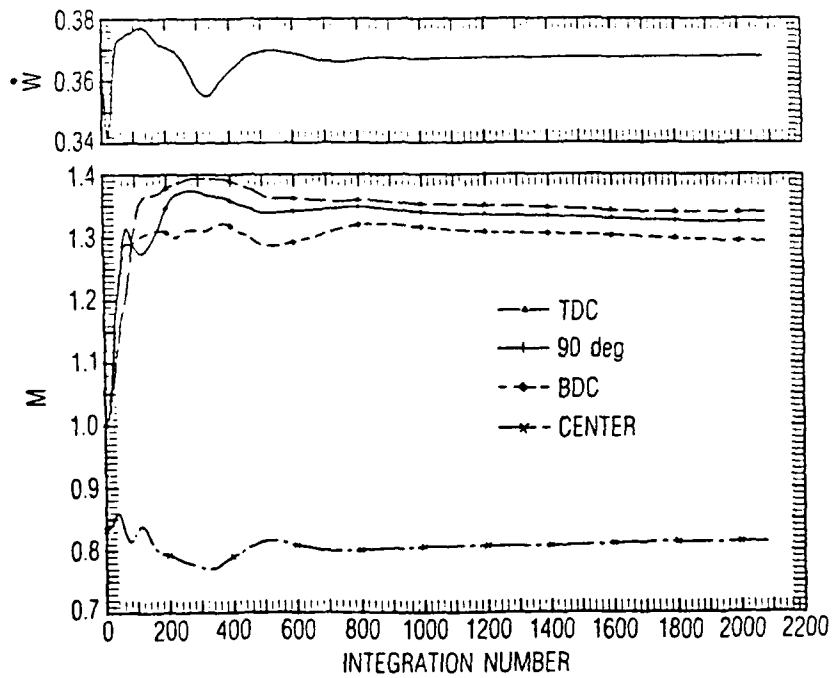


Figure 10. Throat M and \dot{W} at Every Integration Step (one-phase, $\gamma = 1.4$)

The transonic flow field in the vicinity of nozzle throat converges rapidly. It is the resolution of the motor subsonic flow field which consumes most of the machine calculation time. The convergence criterion used in the transonic flow regime requires that the difference in mass flow rate and in Mach number on TDC, 90°, BDC, and centerline at the nozzle throat be less than 0.001% for three consecutive time integration steps. The vectorized computer program developed under this study with 40 x 18 x 13 grid points in the motor and 20 x 18 x 13 in the nozzle flow regions takes up 1.1 million words memory on a CRAY X-MP14 super computer. The converged Titan IV one-phase cold flow transonic solution takes 2083 integration steps which require 4 min, 54 sec computation time. The computed three-dimensional nozzle cold flow discharge coefficient is 0.9855, based on a converged three-dimensional gas mass flow rate of 2.997 lb/sec and a one-dimensional isentropic gas mass flow rate of 3.041 lb/sec at the nozzle throat for the 4.65% scale cold flow model.

The Mach number distributions on the wall and along the centerlines are depicted in Figure 11. It shows that, as flow approaches the motor-nozzle interface plane, higher Mach number occurs on the TDC wall surface with steeper slope change than that on the BDC wall surface. The three-dimensionality of flow is evident from these calculated Mach number distributions. The computed Mach numbers at the throat are 1.339, 1.324, 1.293, and 0.813 at TDC, 90°, BDC, and centerline, respectively, for the cold flow with $\gamma = 1.4$. The results of a single one-dimensional analysis at TDC + 90° plane are also shown in the figure for comparison. It clearly indicates the inadequacy of the one-dimensional analysis applied to a three-dimensional configuration. For the Titan IV nozzle which is canted from BDC toward TDC, the higher pressure load associated with lower flow speed on the BDC plane than that on the TDC plane of the nozzle is to be expected. Shown on the same figure are the data obtained from the cold flow test (Ref. 18). In general, the results of the present three-dimensional flow analysis are in very good agreement with cold flow test data, except in the low speed compression corner region of the aft closure, where the boundary layer is thick and viscous effects prevail.

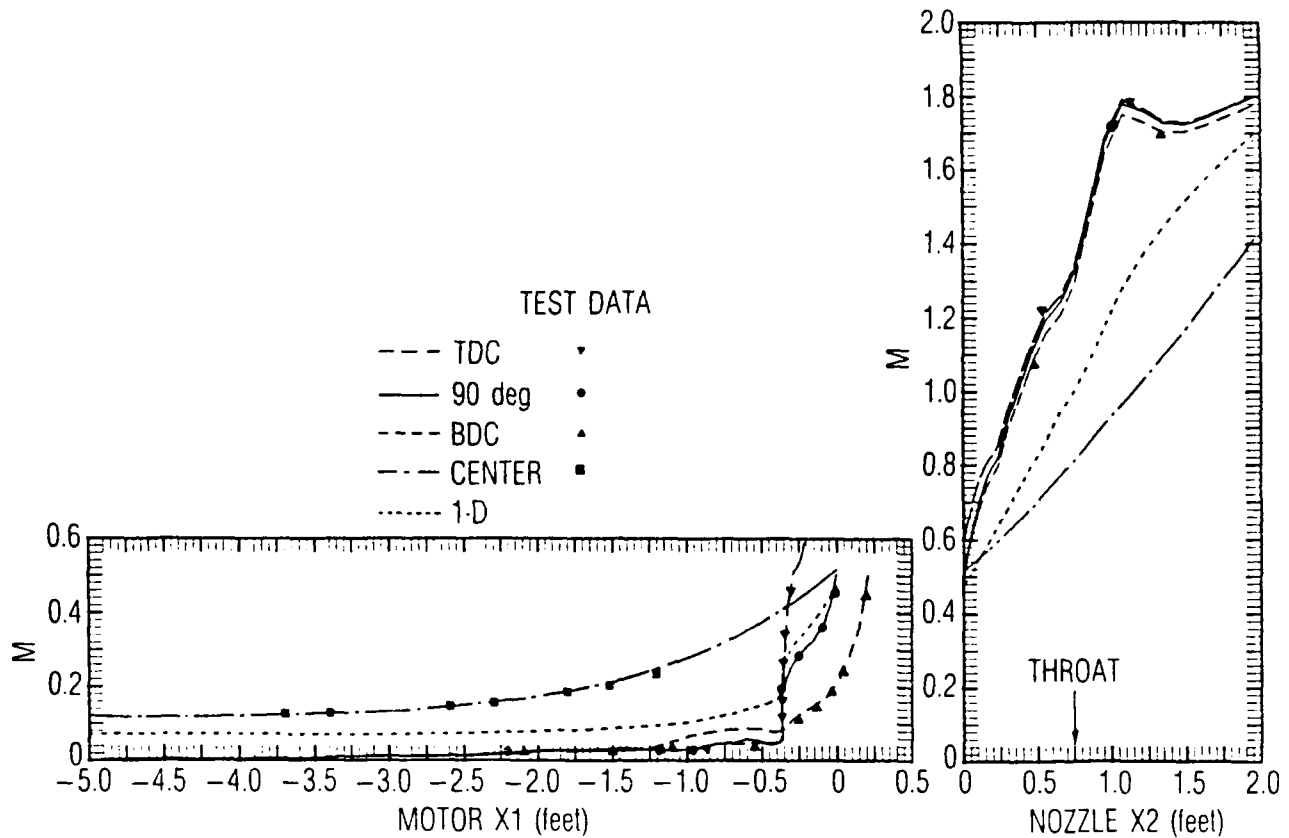


Figure 11. Gas Mach Number Distribution (one-phase, $\gamma = 1.4$)

Figure 12 shows the computed Mach number contour on the TDC-BDC symmetry plane. An isometric projection of the three-dimensional Mach number contour plot is given in Figure 13 for a clear visualization of the computed overall three-dimensional flow field. The sonic surface in the nozzle is marked in Figures 12 and 13. This sonic condition is of particular interest to rocket nozzle designers, not only because it provides a "sonic barrier" beyond which an efficient supersonic marching scheme or method of characteristics is applicable and shock waves usually emerge, but also it is the state at which maximum convective heating occurs at the nozzle wall. Downstream of the sonic state, flow density and pressure decrease drastically, often resulting in reduced convective heating to the nozzle wall.

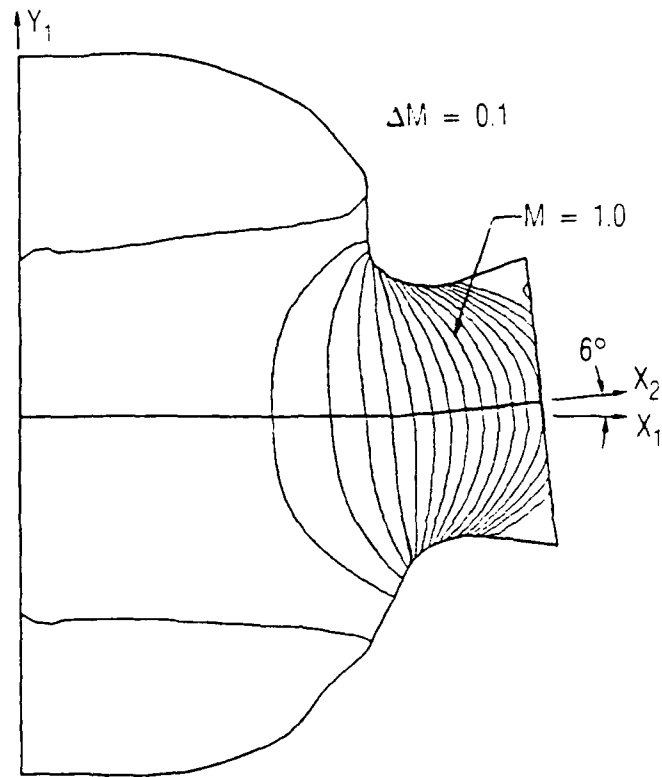


Figure 12. Mach Number Contour on Symmetry Plane (one-phase, $\gamma = 1.4$)

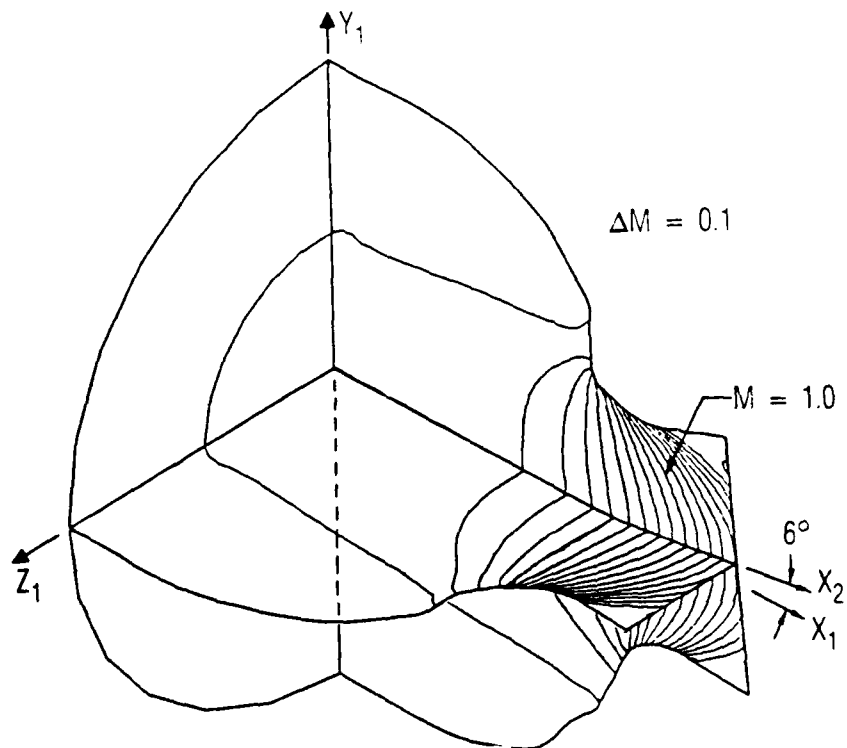


Figure 13. Three-Dimensional Mach Number Contour (one-phase, $\gamma = 1.4$)

Note that the Mach number contour curves are a direct reflection of the calculated three-dimensional flow field from the present analysis and are obtained directly from a Calcomp pen plotter based on the information stored in magnetic tapes. The smoothness of the contour curves and near-normal intersection of the curves with centerlines of the motor and nozzle indicate that the numerical scheme used in the present analysis for boundary treatment works well. Similar to that discussed in Reference 7, a small recompression zone occurs at the wall in the supersonic flow region of the Titan IV nozzle, because of overexpansion of the flow downstream of the throat, which was also observed in the cold flow test.

8. ONE-PHASE HOT FLOW, $\gamma = 1.19$

Based on the assumption that the measured cold flow Mach number at the motor inlet plane is applicable to a full-scale hot firing, the one-phase numerical calculation for a combustion gas ($\gamma = 1.19$) at chamber temperature 5900°R and chamber pressure 570 psia (78.5 sec into the burn) in the Titan IV SRM is also carried out. The assumption is valid from the following observations:

- a. The flow is insensitive to a Reynolds number change from a chamber pressure of 45 psia to 150 psia in the cold flow test.
- b. At the motor inlet plane, the one-dimensional Mach number difference between $\gamma = 1.4$ and $\gamma = 1.19$ is less than 2.4% at the same area ratio = 8.20.
- c. The Mach number at the motor inlet plane is very small; the axisymmetric calculations from a characteristic formulation for the inlet flow in Reference 7 indicates that the difference in Mach number at the motor inlet plane for gases with $\gamma = 1.4$ and $\gamma = 1.19$ is negligible.

The converged Titan IV one-phase hot flow transonic solution takes 2168 integration steps which require 5 min, 7 sec computation time on a CRAY X-MP14 machine. The computed three-dimensional nozzle hot flow discharge coefficient is 0.9850, based on a converged three-dimensional gas mass flow rate of 3920.07 lb/sec and a one-dimensional isentropic gas mass flow rate of 3979.64 lb/sec for the full-scale Titan IV motor with eroded throat diameter 3.3958 ft at 78.5 sec into the burn. The computed Mach numbers at the throat are 1.305, 1.292, 1.266, and 0.824 at TDC, 90°, BDC, and centerline, respectively, for the hot flow with $\gamma = 1.19$.

An isometric projection of a three-dimensional Mach number contour is given in Figure 14. In general, the overall three-dimensional flow structure for the hot firing with $\gamma = 1.19$ is similar to that of the cold flow with $\gamma = 1.4$. Changing γ from 1.4 to 1.19 has the effect of decreasing the Mach number at supersonic speed and increasing the Mach number at subsonic speed. Note that the Titan IV SRM nozzle has a larger and flatter throat, hence a lower throat wall Mach number, than that of the Titan III SRM nozzle discussed in Reference 7.

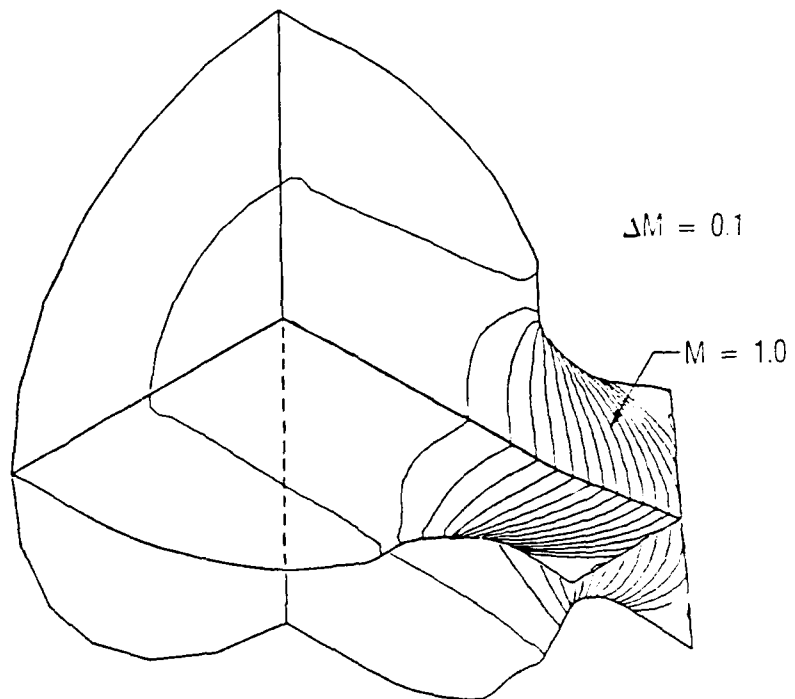


Figure 14. Three-Dimensional Mach Number Contour (one-phase, $\gamma = 1.19$)

9. TWO-PHASE HOT FLOW, GAS $\gamma = 1.19$

The two-phase flow property data for the Titan IV are shown in Table 1. The computed results from the one-phase $\gamma = 1.19$ hot firing are taken to be the initial guess for the fully coupled, gas-particle, two-phase flow analysis. For the two-phase hot flow with a single particle size of $6 \bar{\mu}$ radius in the flow field, the converged solution with a very small convergence criterion of 0.001% requires 5864 integration steps and 40 min computation time on a CRAY X-MP14 super computer. Increasing the convergence criterion to 0.005% will significantly reduce the required computation time to less than 10 min. The discharge coefficient is found to be 1.1764, based on a computed three-dimensional total mass flow rate 4681.59 lb/sec (gas-phase 3348.29 lb/sec + particle phase 1333.30 lb/sec) and a one-dimensional isentropic gas mass flow rate 3979.64 lb/sec. The discharge coefficient is greater than one, when a two-phase mass flow rate is compared with a one-dimensional gas mass flow rate. The computed gas-phase Mach numbers at the throat are 1.152, 1.096, 1.092, and 0.721 at IDC, 90°, EDC, and centerline, respectively, for the two-phase hot flow. The gas-phase Mach number contours for the two-phase hot flow are given in Figures 15 and 16, where the sonic surfaces for both one- and two-phase flows are shown for comparison. With the presence of particles in the flow region, gas-phase expansion is slowed down significantly. The Mach number in the present two-phase study is evaluated from the local sonic speed for the gas-phase with $\gamma = 1.19$. The Mach number will be approximately 2% higher than that shown in this report, if it is computed from a local sonic speed corresponding to an equilibrium gas-particle mixture (EGPM) of $\gamma = 1.152$ based on the equation shown in Reference 7.

Table 1. Titan IV Flow Property Data

<u>Gas Phase</u>	<u>Particle Phase</u>
$\bar{C}_p = 2.68 \text{ KJ/Kg-}^\circ\text{K} (0.64 \text{ Btu/lb}_m - ^\circ\text{R})$	$\bar{C}_j = 1.38 \text{ KJ/Kg-}^\circ\text{K} (0.33 \text{ Btu/lb}_m - ^\circ\text{R})$
$\bar{\mu}_{tl} = 8.88 \times 10^{-5} \text{ Pa-s} (5.97 \times 10^{-5} \text{ lb}_m/\text{ft-s})$	$\bar{m}_j = 3203.69 \text{ Kg/m}^3 (200 \text{ lb}_m/\text{ft}^3)$
$Pr = 0.45$	$\phi = 28.8\%$
$a = 0.664$	$\bar{r}_j = 6\bar{\mu}$
$\gamma = 1.19$	

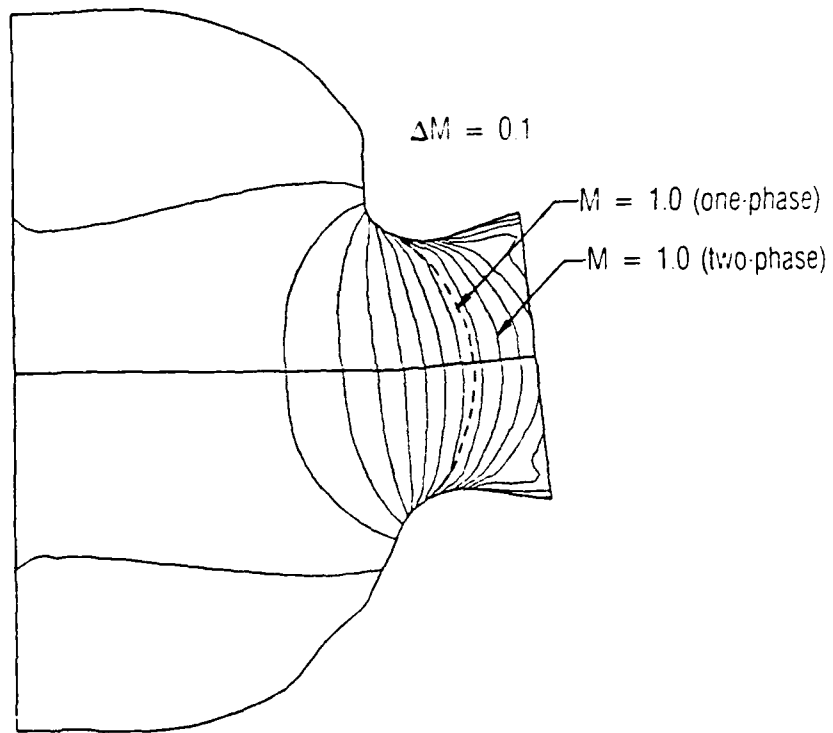


Figure 15. Mach Number Contour on Symmetry Plane (two-phase, $\gamma = 1.19$)

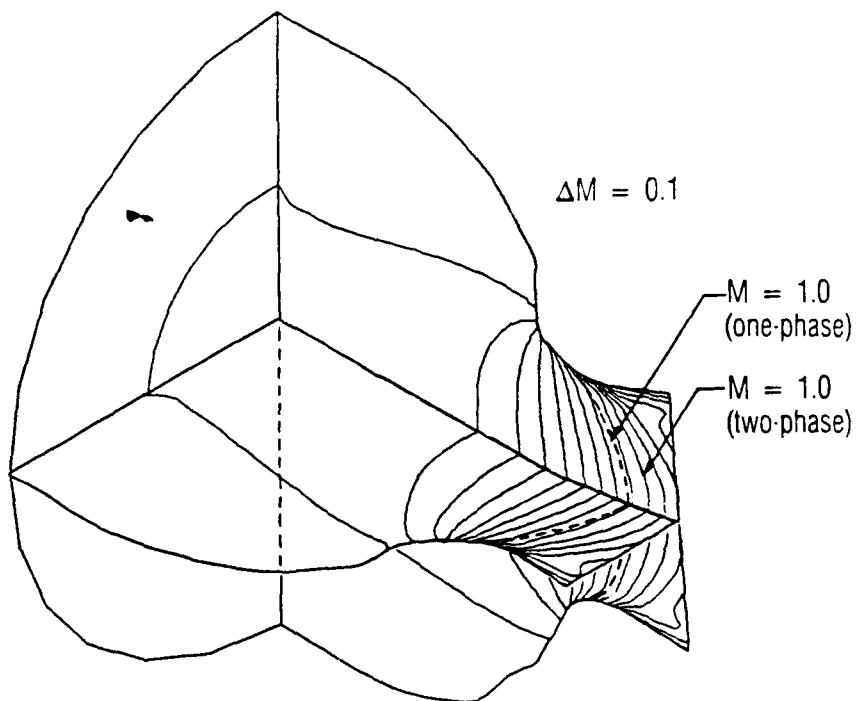


Figure 16. Three-Dimensional Mach Number Contour (two-phase, $\gamma = 1.19$)

Figures 17 through 20 summarize and compare the Mach number and pressure distribution on the wall and centerlines of motor and nozzle flow region for one-phase cold flow, one-phase hot flow, and two-phase hot flow. Although the difference in flow variables between the one-phase cold flow ($\gamma = 1.4$) and the hot flow ($\gamma = 1.19$) is negligible in the low subsonic motor flow region, it cannot be ignored in the transonic and supersonic nozzle flow region. The difference is more pronounced when the particles are introduced into the flow. A higher pressure load on the nozzle wall from the hot flow than that from the cold flow is evident from the results of analysis. The design of solid rocket motor/nozzle and evaluation of motor performance, therefore, should not rely entirely on the data obtained from the cold flow test.

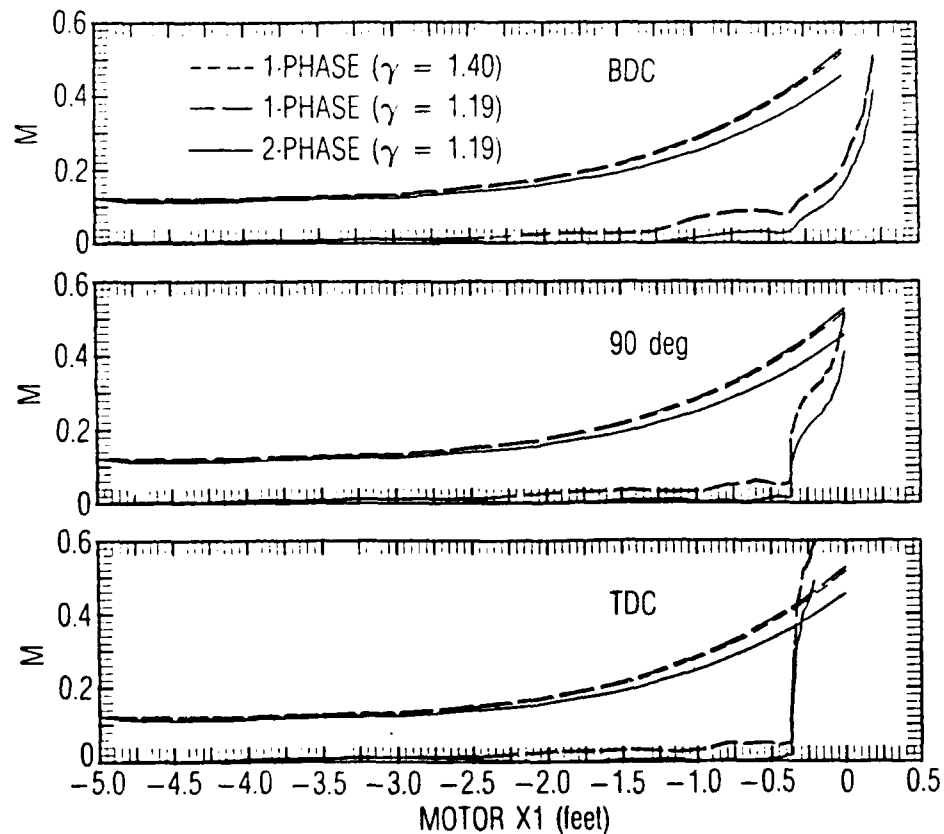


Figure 17. Comparison of Mach Number Distributions (motor)

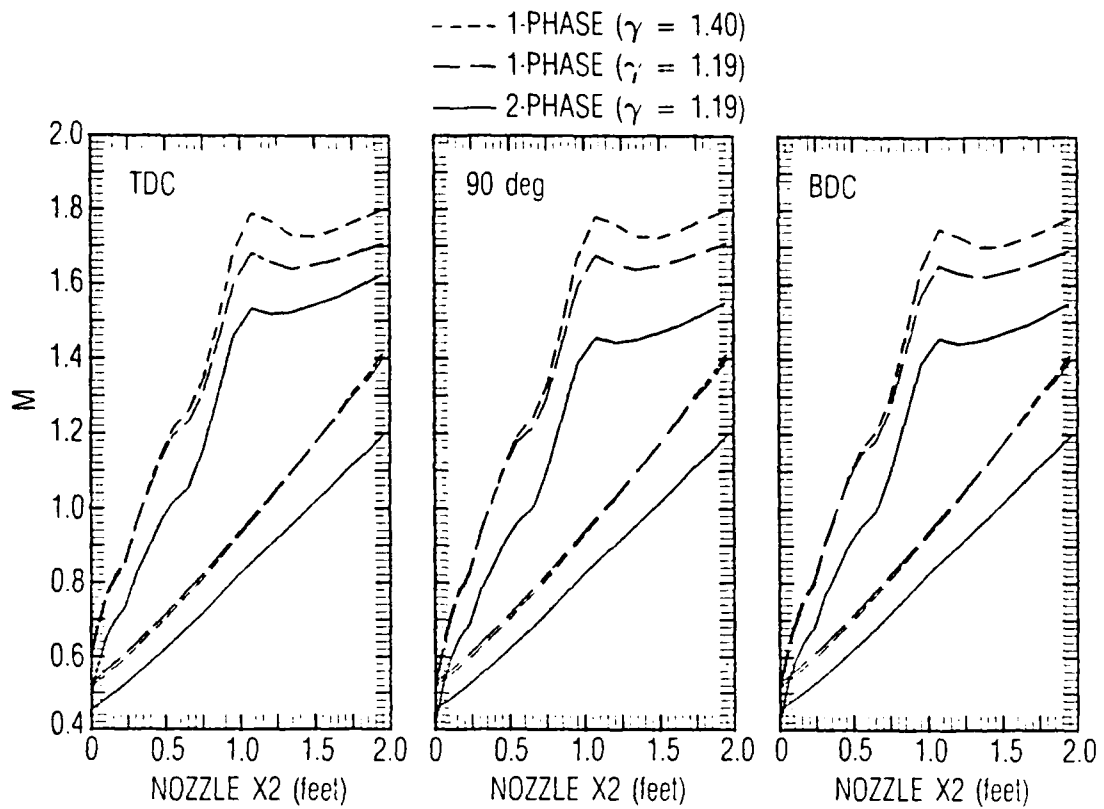


Figure 18. Comparison of Mach Number Distributions (nozzle)

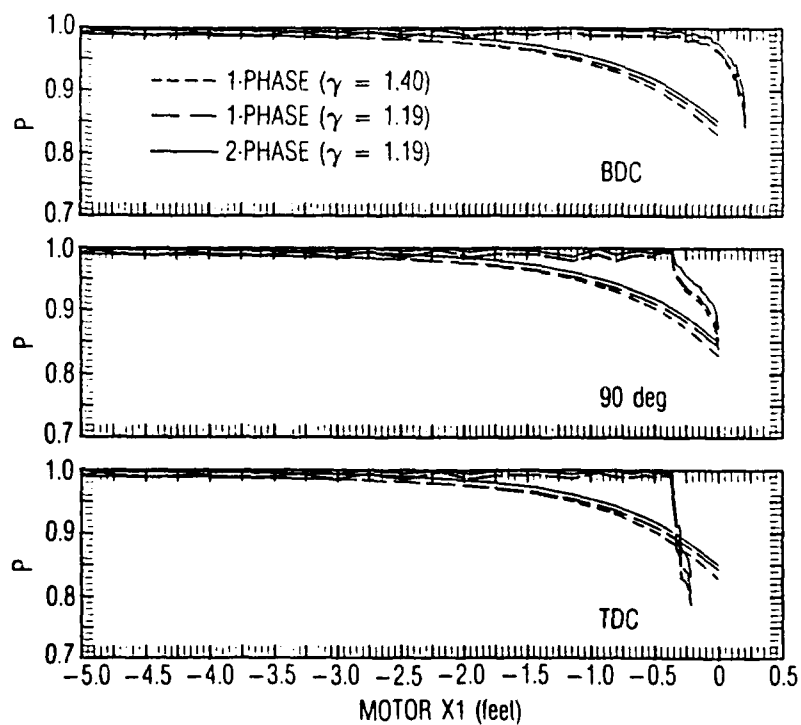


Figure 19. Comparison of Pressure Distributions (motor)

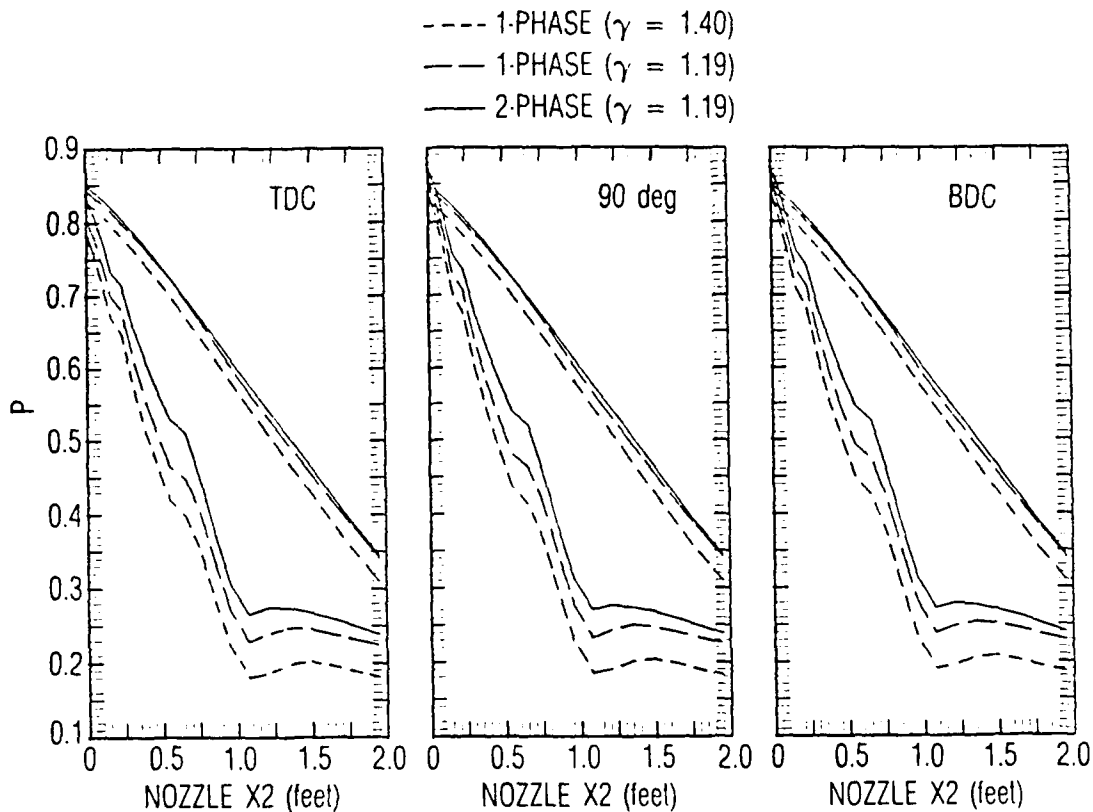


Figure 20. Comparison of Pressure Distributions (nozzle)

For a giant motor like Titan IV (10 ft dia, 113 ft long), it is important to have accurate information on total pressure drop from the forward end of the motor to the aft closure. In a motor firing test, the forward end pressure can be conveniently measured (usually through the igniter boss). But aft closure total pressure is usually unknown, even though it is the aft closure total pressure that directly affects performance and payload delivery capability of a motor, especially during ground level vehicle liftoff. An empirical approach has been taken in the past for calculating the total pressure loss factor with only limited success. A cold flow test, although providing useful information, is often carried out in a benign gas-only one-phase flow environment and is limited to the number of propellant burn-back surfaces that can be simulated. In this regard, if static pressure in the Liquid Injection Thrust Vector Control (LITVC) ports, located in the exit cone downstream of the nozzle throat, is monitored during full-scale Titan IV

static tests, then numerical calculation based on the present analysis can be iteratively applied for defining the aft closure pressure field corresponding to the measured static pressure at downstream exit cone locations.

The gas-phase velocity vector plot on the symmetry plane is presented in Figure 21. A three-dimensional isometric projection of the gas-phase velocity vector plot is given in Figure 22. These velocity plots illustrate that the gas flow aligns itself from the chamber toward the nozzle and then follows the general trend of canting direction.

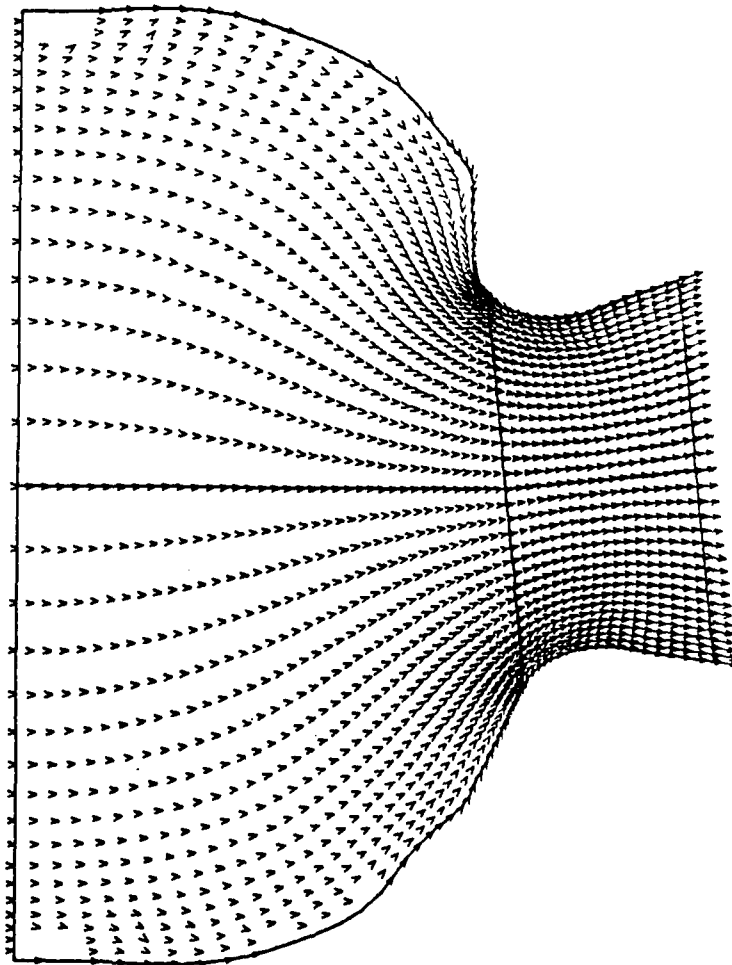


Figure 21. Gas Velocity Vectors on Symmetry Plane (two-phase, $\gamma = 1.19$)

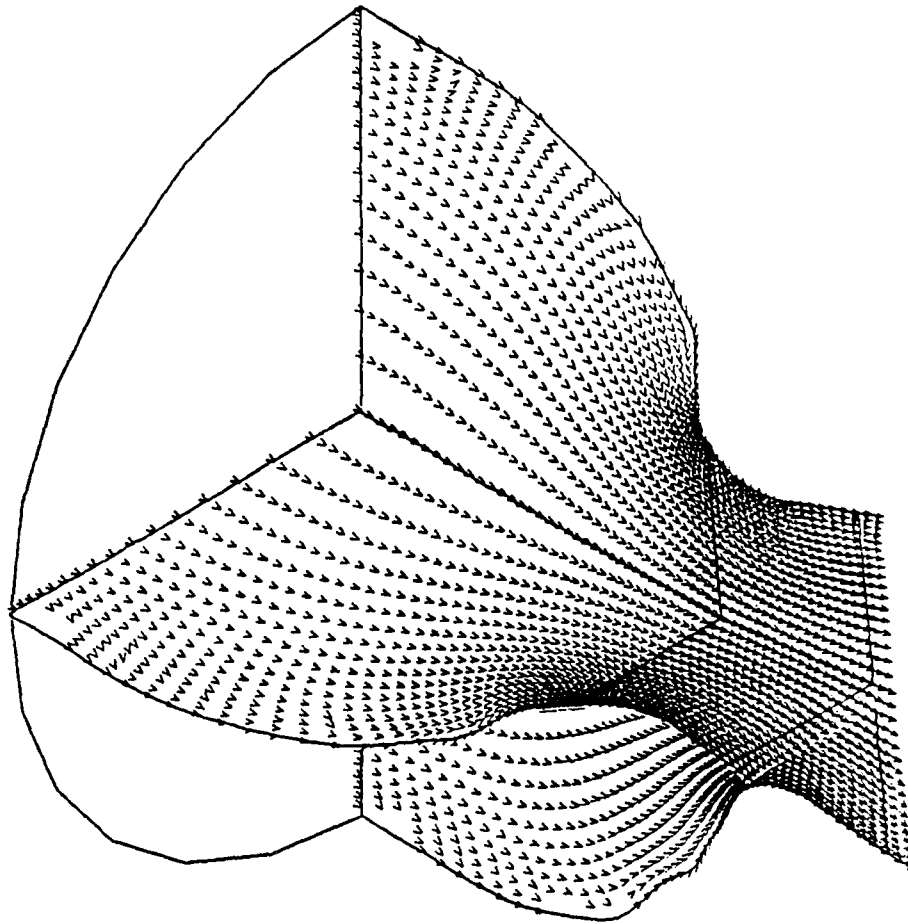


Figure 22. Three-Dimensional Gas Velocity Vectors (two-phase, $\gamma = 1.19$)

The three-dimensional feature of two-phase flow in the Titan IV SRM is portrayed in the particle density contours and particle velocity vector plots of Figures 23 through 26. Since a particle flow path cannot faithfully follow a steep change in wall slope, particles are clustered near the wall with a steep entrance angle. In the nozzle flow region, particle density on the wall differs greatly from TDC to BDC plane, revealing the influence of non-axisymmetric boundary geometry on particle flow path. A distinctive particle-free zone appears in the calculated results. On the TDC wall with a steep slope change, the particle-free zone occurs upstream of the throat. On the BDC wall with a gradual slope change, the particle-free zone occurs downstream of the throat. Moreover, since heavy particles cannot effectively turn around the corner of the nozzle entrance wall with a steep slope change and tend to cluster near the centerline of the nozzle, significant reduction in gas-phase velocity in the two-phase flow from that in the one-phase flow at the centerline near the nozzle exit plane is observed.

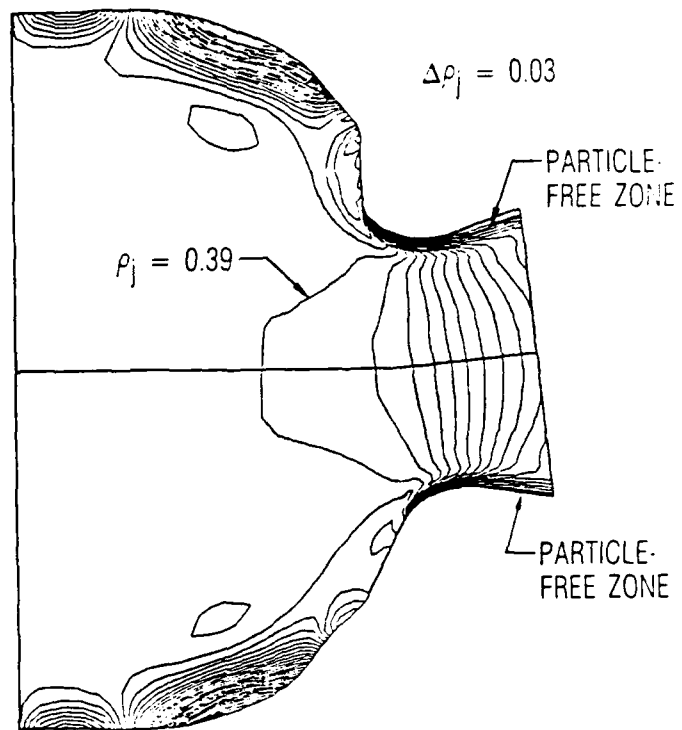


Figure 23. Particle Density Contour on Symmetry Plane (two-phase, $\gamma = 1.19$)

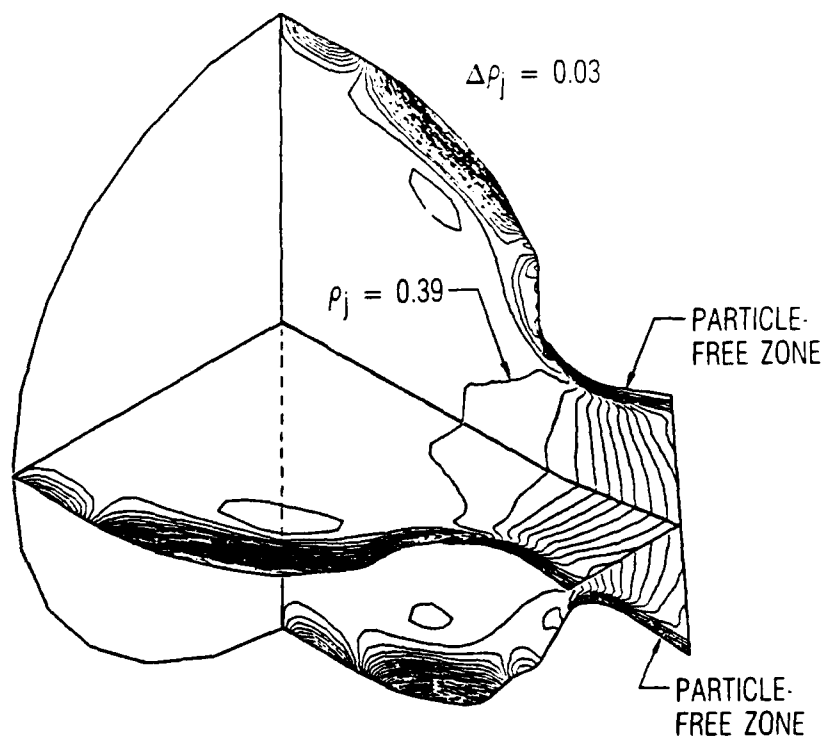


Figure 24. Three-Dimensional Particle Density Contour (two-phase, $\gamma = 1.19$)

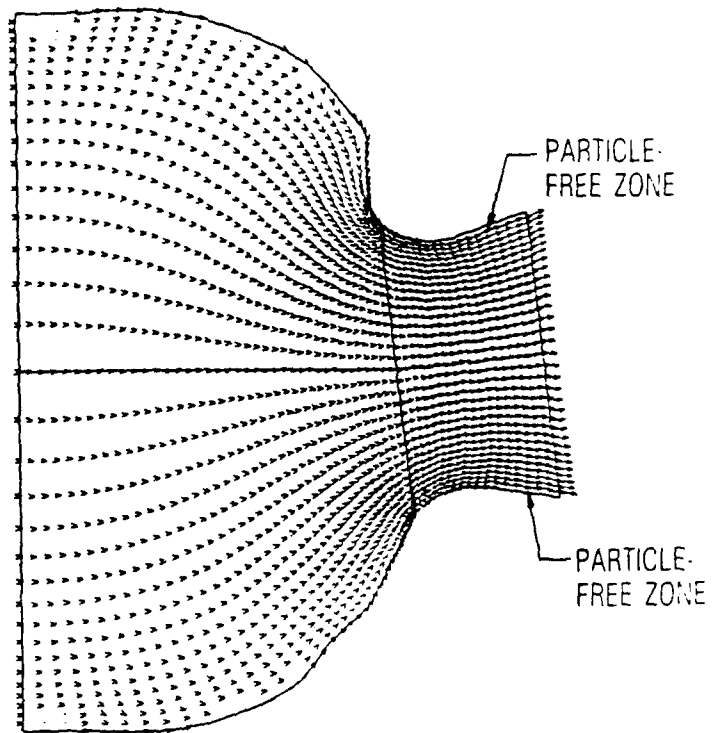


Figure 25. Particle Velocity Vectors on Symmetry Plane
(two-phase, $\gamma = 1.19$)

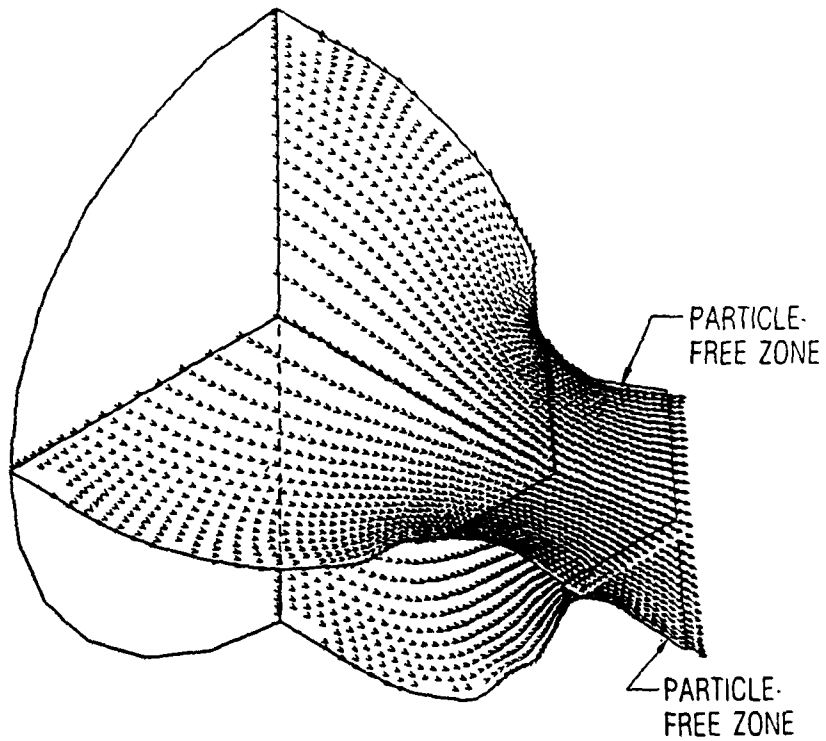


Figure 26. Three-Dimensional Particle Velocity Vectors
(two-phase, $\gamma = 1.19$)

The particle velocity lag λ_q and gas-to-particle temperature ratio λ_T on the nozzle throat plane and the nozzle exit plane are given in Figure 27. On the nozzle throat plane, λ_q and λ_T are higher at the centerline than those near the wall. On the nozzle exit plane, the reverse is true because of gas-phase recompression near the wall downstream of the throat, which reduces the magnitude of relative speed between gas-phase and particle-phase. Clustering of particles near the nozzle centerline downstream of the throat also causes reduction in gas-phase speed, resulting in a slight increase of λ_q from nozzle throat to exit plane. Incidentally, the particle Reynolds number, which is a measure of the magnitude of relative speed between gas-phase and particle-phase, varies from 0 on the motor entrance plane to 17 (TDC), 20 (90°), 21 (BDC), 15 (centerline) on the nozzle entrance plane, to 295 (TDC), 31 (90°), 31 (BDC), 20 (centerline) on the nozzle throat plane and to 247 (TDC), 233 (90°), 235 (BDC), 18 (centerline) on the nozzle exit plane. In the particle-free zone, the particle velocity is zero and the particle Reynolds number becomes the Reynolds number based on the gas speed and a reference particle radius.

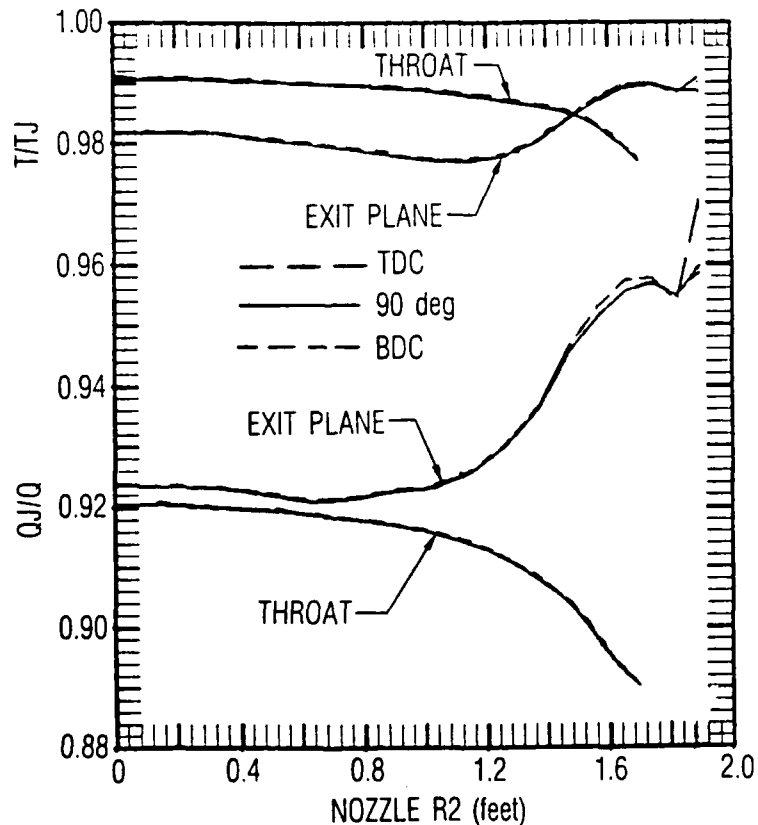


Figure 27. Particle Velocity Lag and Temperature Ratio (nozzle)

The particle-phase flow fields presented in Figures 23 through 27 are useful to rocket nozzle designers for particle impact erosion calculations. Insulation materials such as silica fiber and asbestos filler-loaded nitrile butadiene rubber (NBR) aft closure insulation, graphite-phenolic nozzle throat, and silica-phenolic exit cone and exit cone extension used in the Titan IV SRM provide thermal protection for motor metallic structural components. Adequate insulation design without undue weight penalty is important to vehicle survivability in a hostile launching environment. An investigation of enhanced insulation erosion from particle impact usually requires knowledge of incident particle density, flow angle, and velocity. This information can be obtained directly from a fully coupled, two-phase analysis such as the one shown in this report.

Finally, a post-processor was recently developed for automated color display of the computational results from the present analysis. Figures 28 and 29 compare the color three-dimensional Mach number contours for the gas-only one-phase and fully coupled gas-particle two-phase flows inside the Titan IV SRM. The lines in these figures are portions of the interior computational grid. The numbers next to the color chart indicate contour values. As mentioned previously, the Mach number for a two-phase flow is lower than for a one-phase flow and can be seen from these figures. The color three-dimensional pressure contours (Fig. 30) show that the pressure remains essentially unchanged on most of the aft closure interior surface and drops rapidly in the throat region of the nozzle. The overall pressure load on the aft closure and nozzle is higher for the two-phase flow than for the one-phase flow. The pressure distribution shown here is required for motor performance and thermostructural analysis. The color three-dimensional particle density contours (Fig. 31) reveal high concentration of particles near concave regions of the aft closure, indicating high local insulation erosion. This has been confirmed by the data from two full-scale Titan IV static motor tests and partially explains the burn-through failure in this area of the first seven-segment MOL test motor 19 years ago.

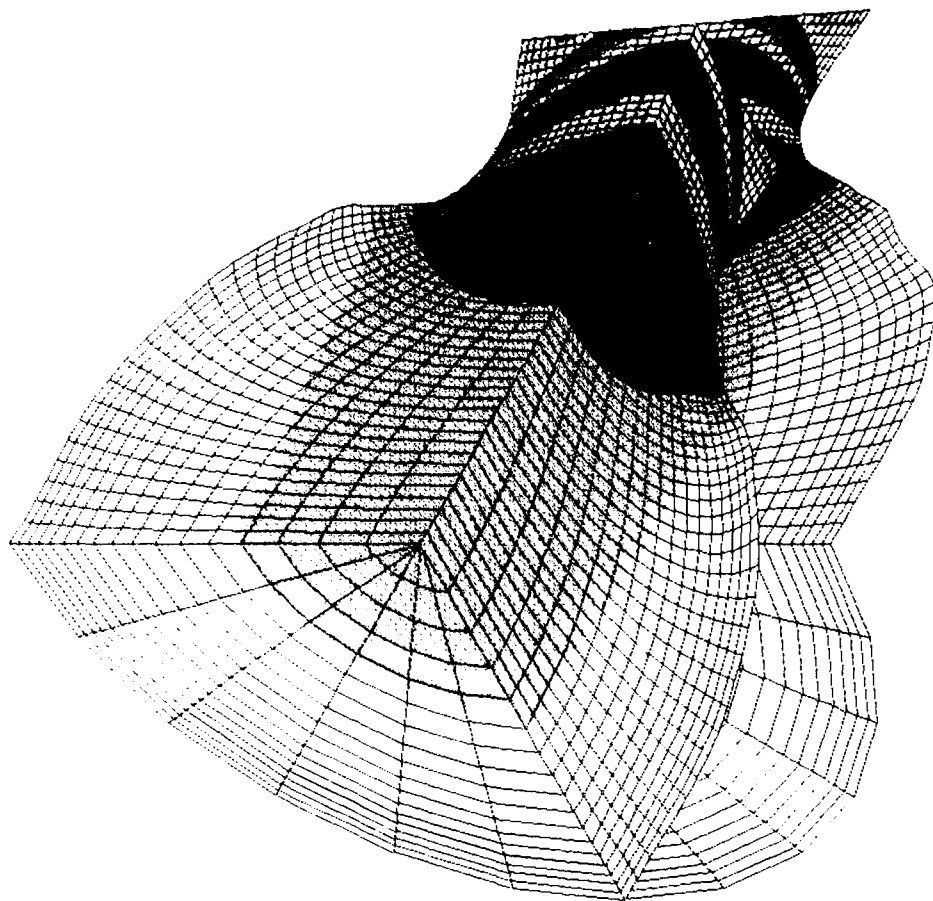
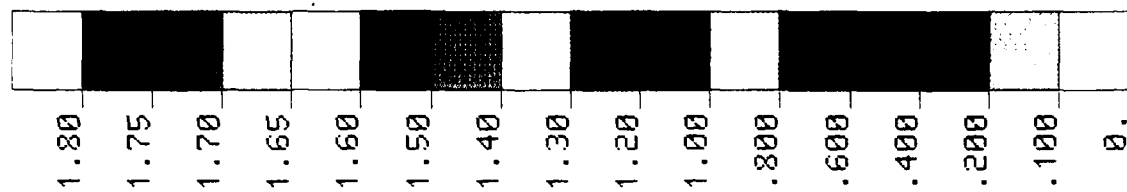


Figure 28. Three-Dimensional Mach Number Contour, Titan IV Solid Rocket Motor (one-phase flow, $\gamma = 1.19$)

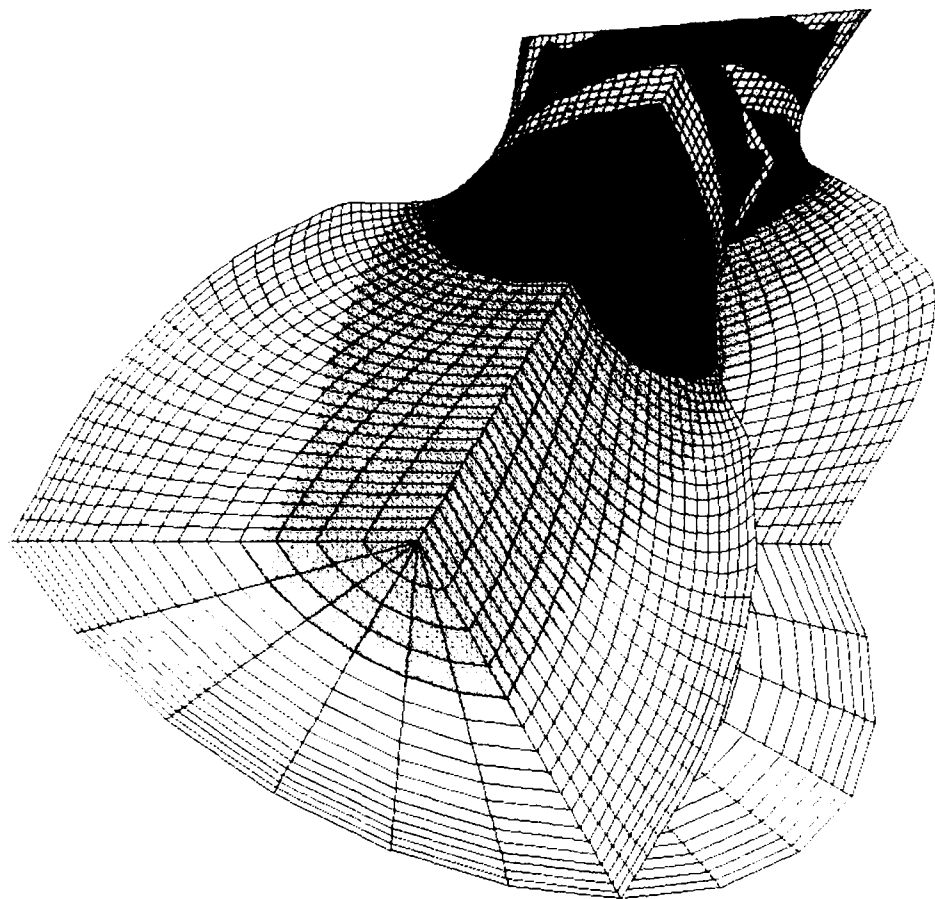
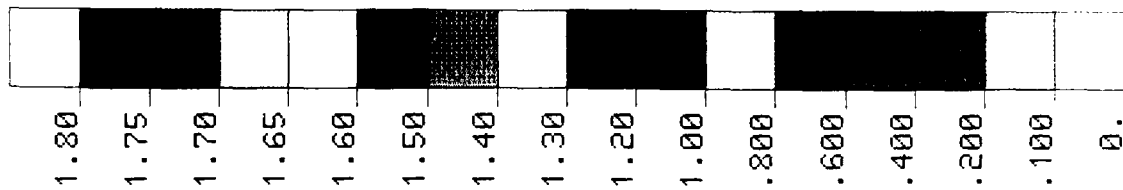


Figure 29. Three-Dimensional Mach Number Contour, Titan IV Solid Rocket Motor (two-phase flow, $\gamma = 1.19$)

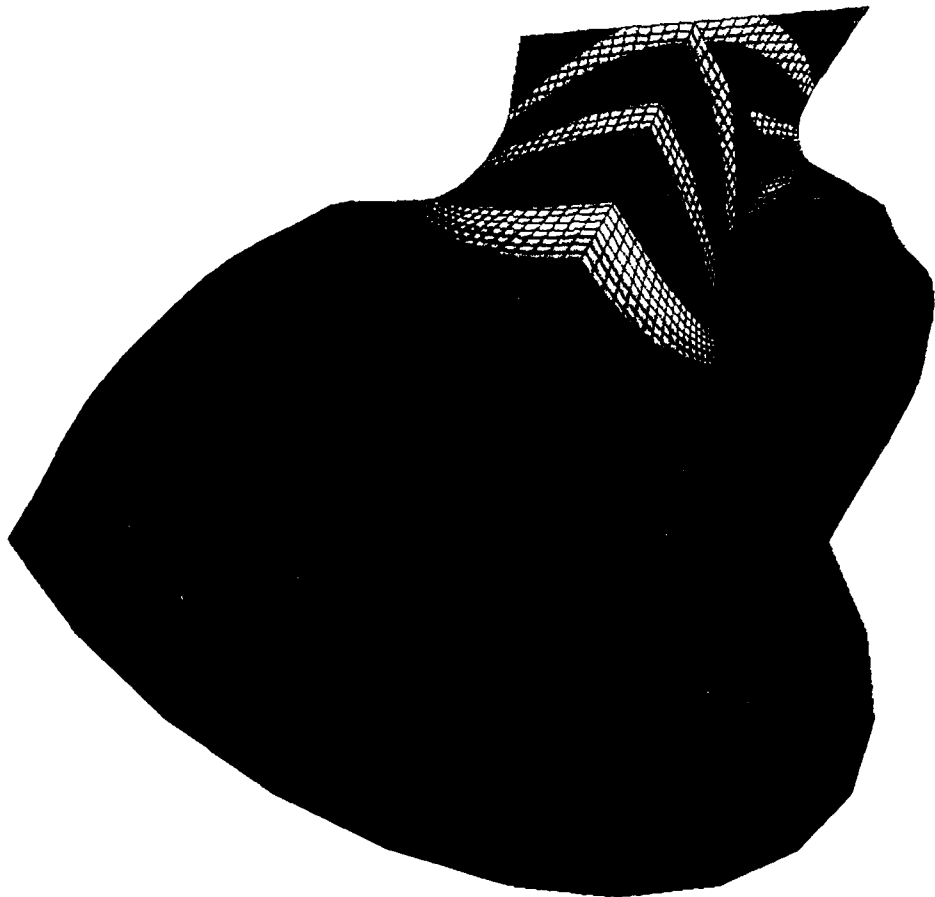
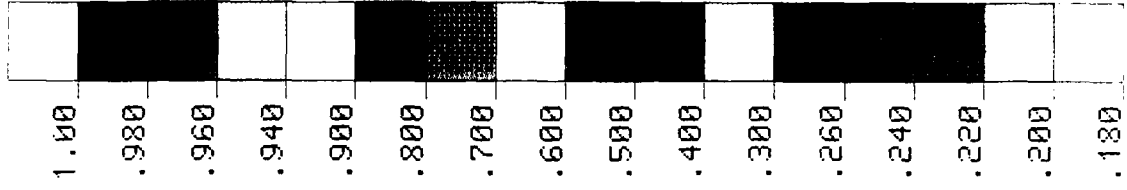


Figure 30. Three-Dimensional Gas Pressure Contour, Titan IV Solid Rocket Motor (two-phase flow, $\gamma = 1.19$)

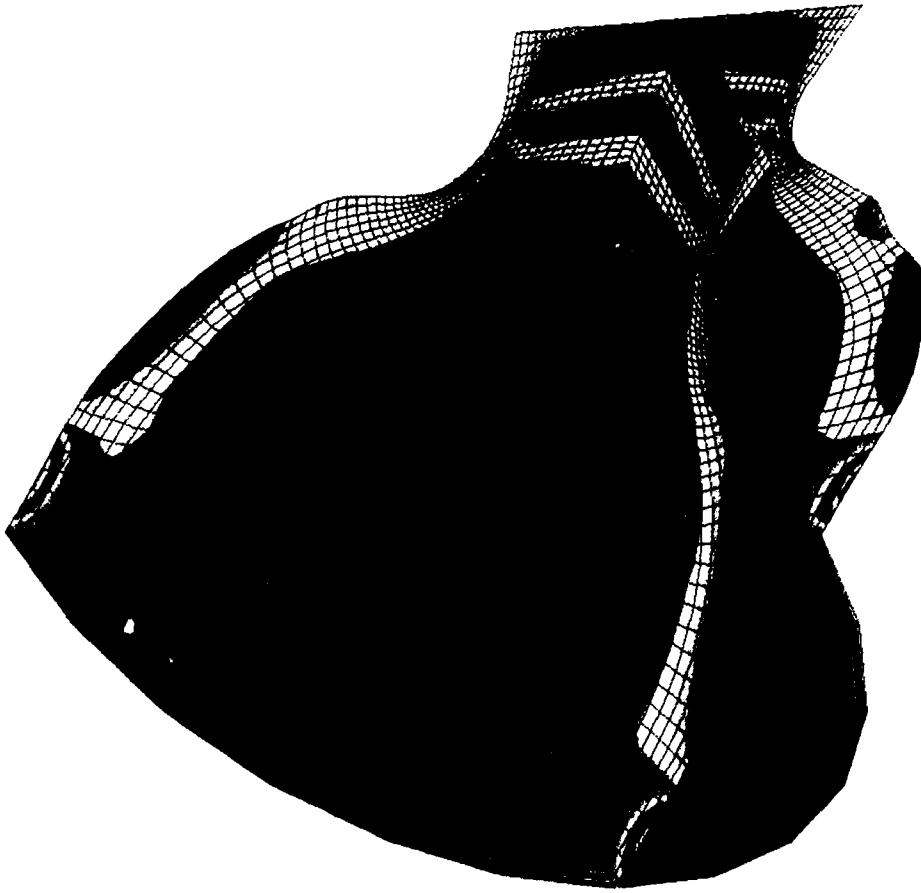
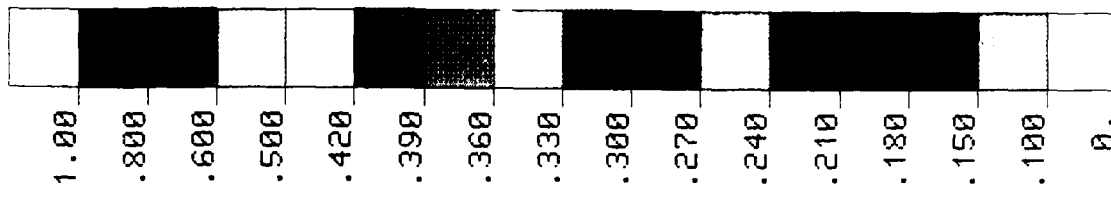


Figure 31. Three-Dimensional Particle Density Contour, Titan IV Solid Rocket Motor (two-phase flow, $\gamma = 1.19$)

10. CONCLUSIONS

In this study, the treatment of complicated three-dimensional motor and nozzle geometries is facilitated through use of three-dimensional, body-fitted grid systems. Difficulty and confusion associated with a canted nozzle due to different sets of reference coordinates are eliminated through introduction of multiple flow regions which allow precise interpretation of flow variables in each region. The idealized fully coupled, gas-particle, two-phase flow governing equations in three-dimensional space are solved numerically. Cold flow test data are utilized for verification of the operational computer program which is developed from a careful numerical consideration. Results of the analysis are presented for a rocket motor of practical importance in space exploration. Important features of compressible nozzle flows are discussed; namely, gas-only, one-phase flows with different ratios of specific heats and a fully coupled, gas-particle, two-phase flow inside a canted three-dimensional Titan IV SRM. The groundwork laid herein will be helpful to the further study of viscous, three-dimensional, multi-particle sized, two-phase nozzle flows.

REFERENCES

1. "3-D Computation Techniques Applied to Internal Flows in Propulsion Systems," AGARD Lecture Series No. 140, May 1985.
2. Kliegel, J. R., "One-Dimensional Flow of a Gas Particle System," IAS Paper No. 60-5, Jan. 1960.
3. Bailey, W. S. et al., "Gas Particle Flow in an Axisymmetric Nozzle," ASR Journal, June 1961, pp. 793-798.
4. Kliegel, J. R., "Gas Particle Nozzle Flows," Ninth (International) Symposium on Combustion, Academic Press, New York, 1963, p. 811.
5. Regan, J. F., H. D. Thompson, and R. F. Hogland, "Two-Dimensional Analysis of Transonic Gas-Particle Flows in Axisymmetric Nozzles," Journal of Spacecraft and Rockets, 8, Apr. 1971, pp. 346-351.
6. Rudinger, G., "Flow of Solid Particles in Gases," AGARD-AG-222, Oct. 1976.
7. Chang, I-Shih, "One- and Two-Phase Nozzle Flows," AIAA Journal, 18(12), Dec. 1980, pp. 1455-1461; AIAA paper 80-0272.
8. Chang, I-Shih, "Three-Dimensional, Two-Phase Supersonic Nozzle Flows," AIAA Journal, 21(5), May 1983, pp. 671-678.
9. Mastin, C. W. and J. F. Thompson, "Transformation of Three-Dimensional Regions onto Rectangular Regions by Elliptic Systems," Numerische Mathematik, 29, pp. 397-407, 1978; also ICASE Report 76-13, 26 Apr. 1976.
10. Mastin, C. W. and J. F. Thompson, "Three-Dimensional Body-Fitted Coordinate Systems for Numerical Solution of the Navier-Stokes Equations," AIAA Paper 78-1147, July 1978.
11. Henderson, C. B., "Drag Coefficients of Spheres in Continuum and Rarefied Flows," AIAA Journal, 14, June 1976, p. 707.
12. Carlson, D. J. and R. F. Hogland, "Particle Drag and Heat Transfer in Rocket Nozzles," AIAA Journal, 2, Nov. 1964, p. 1980.
13. Viviani, H., "Formes Conservatives des Équations de la Dynamique des Gaz," La Recherche Aéronautique, Année 1974, 1 (Janvier-Février), pp. 65-66.
14. MacCormack, R. W., "The Effect of Viscosity in Hyper Velocity Impact Cratering," AIAA Paper 69-354, May 1969.
15. Serra, R. A., "Determination of Internal Gas Flows by a Transient Numerical Techniques," AIAA Journal, 10, May 1972, pp. 603-611.

REFERENCES (Continued)

16. Phares, W. J., "Computation of Three-Dimensional Transonic Internal Flow in Cylindrical Coordinates," AEDC-TR-80-56, Aug. 1981.
17. Thompson, J. F., F. C. Thames, and C. W. Mastin, "Boundary-Fitted Curvilinear Coordinates Systems for Solution of Partial Differential Equations on Fields Containing Any Number of Arbitrary Two-Dimensional Bodies," NASA CR2729, July 1977; also J. of Computational Physics, 24, 1977, pp. 245-273.
18. Dunlap, R., et al., "Titan IV (CELV/T34D7) Cold Flow Study Report," CSD4001-86-89 Chemical Systems Division, United Technology Center, July 1986.

EDC d0136Q/a1753J

LABORATORY OPERATIONS

The Aerospace Corporation functions as an "architect-engineer" for national security projects, specializing in advanced military space systems. Providing research support, the corporation's Laboratory Operations conducts experimental and theoretical investigations that focus on the application of scientific and technical advances to such systems. Vital to the success of these investigations is the technical staff's wide-ranging expertise and its ability to stay current with new developments. This expertise is enhanced by a research program aimed at dealing with the many problems associated with rapidly evolving space systems. Contributing their capabilities to the research effort are these individual laboratories:

Aerophysics Laboratory: Launch vehicle and reentry fluid mechanics, heat transfer and flight dynamics; chemical and electric propulsion, propellant chemistry, chemical dynamics, environmental chemistry, trace detection; spacecraft structural mechanics, contamination, thermal and structural control; high temperature thermomechanics, gas kinetics and radiation; cw and pulsed chemical and excimer laser development including chemical kinetics, spectroscopy, optical resonators, beam control, atmospheric propagation, laser effects and countermeasures.

Chemistry and Physics Laboratory: Atmospheric chemical reactions, atmospheric optics, light scattering, state-specific chemical reactions and radiative signatures of missile plumes, sensor out-of-field-of-view rejection, applied laser spectroscopy, laser chemistry, laser optoelectronics, solar cell physics, battery electrochemistry, space vacuum and radiation effects on materials, lubrication and surface phenomena, thermionic emission, photo-sensitive materials and detectors, atomic frequency standards, and environmental chemistry.

Computer Science Laboratory: Program verification, program translation, performance-sensitive system design, distributed architectures for spaceborne computers, fault-tolerant computer systems, artificial intelligence, micro-electronics applications, communication protocols, and computer security.

Electronics Research Laboratory: Microelectronics, solid-state device physics, compound semiconductors, radiation hardening; electro-optics, quantum electronics, solid-state lasers, optical propagation and communications; microwave semiconductor devices, microwave/millimeter wave measurements, diagnostics and radiometry, microwave/millimeter wave thermionic devices; atomic time and frequency standards; antennas, rf systems, electromagnetic propagation phenomena, space communication systems.

Materials Sciences Laboratory: Development of new materials: metals, alloys, ceramics, polymers and their composites, and new forms of carbon; non-destructive evaluation, component failure analysis and reliability; fracture mechanics and stress corrosion; analysis and evaluation of materials at cryogenic and elevated temperatures as well as in space and enemy-induced environments.

Space Sciences Laboratory: Magnetospheric, auroral and cosmic ray physics, wave-particle interactions, magnetospheric plasma waves; atmospheric and ionospheric physics, density and composition of the upper atmosphere, remote sensing using atmospheric radiation; solar physics, infrared astronomy, infrared signature analysis; effects of solar activity, magnetic storms and nuclear explosions on the earth's atmosphere, ionosphere and magnetosphere; effects of electromagnetic and particulate radiations on space systems; space instrumentation.